DOI: 10.1021/ic900742q

Inorganic Chemistry
Article

Electrochemical and Electronic Structure Investigations of the $[S_3N_3]^{\bullet}$ Radical and Kinetic Modeling of the $[S_4N_4]^n/[S_3N_3]^n$ ($n = 0, -1$) Interconversion

René T. Boeré,*,† Tristram Chivers,*,‡ Tracey L. Roemmele,†,‡ and Heikki M. Tuononen§

†*Department of Chemistry and Biochemistry, University of Lethbridge, Lethbridge, Alberta, Canada T1K 3M4,* ‡*Department of Chemistry, University of Calgary, Calgary, Alberta, Canada T2N 1N4, and* §*Department of Chemistry, University of Jyväskylä, Jyväskylä, FI-40014, Finland*

Received April 16, 2009

Voltammetric studies of S_4N_4 employing both cyclic (CV) and rotating disk (RDE) methods in CH_2Cl_2 at a glassy carbon electrode reveal a one-electron reduction at −1.00 V (versus ferrocene/ferrocenium), which produces a second redox couple at −0.33 V, confirmed to be the electrochemically generated $[S_3N_3]^-$ by CV studies on its salts. Diffusion coefficients (CH_2Cl_2/0.4 M [^{n}Bu$_4$N][PF_6]) estimated by RDE methods: S_4N_4, 1.17×10^{-5} cm^2 s^{-1}; $[S_3N_3]^-$, 4.00×10^{-6} cm^2 s^{-1}. Digital simulations of the CVs detected slow rates of electron transfer for both couples and allowed for a determination of rate constants for homogeneous chemical reaction steps subsequent to electron transfer. The common parameters ($k_{f1} = 2.0 \pm 0.5$ s^{-1}, $k_{s1} = 0.034 \pm 0.004$ cm s^{-1} for $[S_4N_4]^{-/0}$; $k_{f2} = 0.4 \pm 0.2$ s^{-1}, $k_{s2} = 0.022 \pm 0.005$ cm s^{-1} for $[S_3N_3]^{-/0}$ at $T = 21 \pm 2$ °C) fit well to a "square-scheme" mechanism over the entire range of data with first order decay of both redox products. An alternate model could also be fit wherein $[NS]^{\bullet}$ liberated in the first step reacts with formed $[S_3N_3]^{\bullet}$ to reproduce S_4N_4 with an apparent second order rate constant $k_{f2}' = 1.1 \pm 0.3 \times 10^3$ M^{-1} s^{-1}. The crystal structure of [PPN][S_3N_3] was determined by X-ray crystallography indicating the solvation of the anion by 1 equiv of methanol. The generated $[S_4N_4]^{-\bullet}$ radical anion was detected by the Simultaneous Electrochemical Electron Paramagnetic Resonance (SEEPR) method to give: (a) $[^{32}S_4{}^{14}N_4]^{-\bullet}$, 9 lines, $a(^{14}N) = 0.118$ mT; (b) $[^{32}S_4{}^{15}N_4]^{-\bullet}$, 5 lines, $a(^{15}N) = 0.164$ mT; (c) $[^{33}S_4{}^{14}N_4]^{-\bullet}$, *estimated* $a(^{14}N) = 0.118$, $a(^{33}S = 0.2$ mT); $g = 2.0008(1)$. Equivalence of ^{33}S hyperfine splittings is consistent with dynamic averaging of the C_{2v} geometry in solution. High-level electronic structure calculations provide evidence for an open-shell doublet triradicaloid character to the ground state wave function of $[S_3N_3]^{\bullet}$.

Introduction

Unsaturated binary sulfur−nitrogen (S,N) compounds readily undergo redox reactions that are accompanied by remarkable structural changes, which continue to challenge the emerging understanding of mechanistic pathways in main group chemistry.[1] Despite being formally electron-rich they are often capable of being either oxidized or reduced.[2] Tetrasulfur tetranitride, S_4N_4 (**1**), is the best known member of this class and has been extensively investigated by electrochemistry, electron paramagnetic resonance (EPR) spectroscopy, and density functional theory (DFT) calculations.[3] Its versatility stems from multifaceted chemical behavior whereby it is the source of many other binary sulfur−nitrogen compounds, including the cyclic trisulfur trinitride anion $[S_3N_3]^-$ (**2**) (Chart 1).[4]

The redox chemistry of S_4N_4 has been the subject of numerous studies.[1] Chemical oxidation with reagents such as AsF_5 or HSO_3F produces the cyclic $[S_3N_2]^{+\bullet}$ radical cation[5]

*To whom correspondence may be addressed. E-mail: boere@uleth.ca (R.T.B.), chivers@ucalgary.ca (T.C.). Phone: (403) 329-2045 (R.T.B.), (403) 220-5741 (T.C.). Fax: (403) 329-2057 (R.T.B.), (403) 289-9488 (T.C.).

(1) Chivers, T. *A Guide to Chalcogen-Nitrogen Chemistry*; World Scientific Publishing Co.: Singapore, 2005.
(2) Oakley, R. T. *Prog. Inorg. Chem.* **1988**, *36*, 299–391.
(3) (a) Chapman, D.; Massey, A. G. *Trans. Faraday Soc.* **1962**, *58*, 1291–1299. (b) Meinzer, R. A.; Pratt, D. W.; Myers, R. J. *J. Am. Chem. Soc.* **1969**, *91*, 6623–6625. (c) Williford, J. D.; VanReet, R. E.; Eastman, M. P.; Prater, K. B. *J. Electrochem. Soc.* **1973**, *120*, 1498–1501. (d) Hojo, M. *Bull. Chem. Soc. Jpn.* **1980**, *53*, 2856–2860. (e) Chivers, T.; Hojo, M. *Inorg. Chem.* **1984**, *23*, 1526–1530. (f) Tweh, J. W.; Turner, A. G. *Inorg. Chim. Acta* **1981**, *48*, 173–177. (g) Preston, K .F.; Sutcliffe, L. H. *Magn. Reson. Chem.* **1990**, *28*, 189–204. (h) Tanaka, K.; Yamabe, T.; Tachibana, A.; Kato, H.; Fukui, K. *J. Phys. Chem.* **1978**, *82*, 2121–2126. (i) Chung, G.; Lee, D. *J. Mol. Struct.* **2002**, *582*, 85–90. (j) Scherer, W.; Spiegler, M.; Pedersen, B.; Tafipolsky, M.; Hieringer, W.; Reinhard, B.; Downs, A. J.; McGrady, G. S. *Chem. Commun.* **2000**, 635–636. (k) Villena-Blanco, M.; Jolly, W. L. *Inorg. Synth.* **1967**, *9*, 98–102. (l) Maaninen, A.; Siivari, J.; Laitinen, R. S.; Chivers, T. *Inorg. Synth.* **2002**, *33*, 196–199.
(4) (a) Bojes, J.; Chivers, T. *J. Chem. Soc., Chem. Commun.* **1977**, 453–454. (b) Bojes, J.; Chivers, T.; Drummond, I.; MacLean, G. *Inorg. Chem.* **1978**, *17*, 3668–3672. (c) Bojes, J.; Chivers, T. *Inorg. Chem.* **1978**, *17*, 318–321. (d) Chivers, T.; Laidlaw, W. G.; Oakley, R. T.; Trsic, M. *J. Am. Chem. Soc.* **1980**, *102*, 5773–5781. (e) Bojes, J.; Chivers, T.; Oakley, R. T.; Womershäuser, G.; Schnauber, M. *Inorg. Synth.* **1989**, *25*, 30–35. (f) Jones, R.; Kelly, P. F.; Williams, D. J.; Woollins, J. D. *Polyhedron* **1987**, *6*, 1541–1545. (g) Bojes, J.; Chivers, T.; Laidlaw, W. G.; Trsic, M. *J. Am. Chem. Soc.* **1979**, *101*, 4517–4522.
(5) Gillespie, R. J.; Kent, J. P.; Sawyer, J. F. *Inorg. Chem.* **1981**, *20*, 3784–3799.

 Published on Web 07/09/2009

Chart 1. Chemical Structures for Compounds **1**−**4**

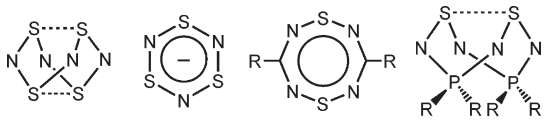

1 **2** **3** **4**

or, in the presence of an excess of the oxidizing agents $SbCl_5$, AsF_5, or $S_2O_6F_2$, the cyclic dication $[S_4N_4]^{2+}$.[6] The radical cation $[S_4N_4]^{+\bullet}$ has not been convincingly characterized. The EPR spectrum of the radical formed on γ−irradiation of S_4N_4 in $CFCl_3$ at 77 K was attributed to $[S_4N_4]^{+\bullet}$, but no ^{14}N hyperfine splitting (hfs) was observed.[7a] A minor product from the reaction of $(NSCl)_3$ with $FeCl_3$ in CH_2Cl_2 was identified as $[S_4N_4]^{+\bullet}[FeCl_4]^-$ on the basis of the X-ray structure;[7] however, the perturbation of the S−N bond lengths in the eight-membered ring is consistent with the formation of the protonated species $[S_4N_4H]^+$.[8] Ring-size changes also accompany the oxidation of S_4N_4 with Cl_2 or SO_2Cl_2 to $S_3N_3Cl_3$ while reduction of the latter reproduces S_4N_4.[1]

Bojes and Chivers provided convincing evidence that the electrolytic reduction of S_4N_4 in anhydrous ethanol produced salts of $[S_3N_3]^-$, while the end product of reduction with potassium metal in dimethoxyethane (DME) is $K[S_3N_3]$.[4b] Previously, Chapman and Massey had reported a surprisingly persistent EPR signal from potassium metal reduction of S_4N_4 in DME at room temperature. They observed a nine-line pattern with the intensity ratio expected from hyperfine splitting (hfs) of 0.322 mT to four equivalent $I = 1$ nuclei, which was attributed to the radical anion $[S_4N_4]^{-\bullet}$.[3a] However, this assignment has been refuted by the work of Meinzer et al.[3b] and Williford et al.[3c] who both reported the generation of a transient EPR signal during low-temperature electrochemical reduction of S_4N_4 in THF/$[^nBu_4N][ClO_4]$ at −25 °C or $CH_3CN/[Et_4N][ClO_4]$ at −20 °C with a much smaller hfs reported to be 0.1185(1) or 0.117(2) mT. In contrast to the 1962 report, neither of the electrochemical studies gave a detectable radical at room temperature; the true origin of the 0.322 mT nine-line pattern thus remains a mystery. Williford et al.[3c] also performed a variable-temperature cyclic voltammetry (CV) study in $CH_3CN/[Et_4N][ClO_4]$ over the range −25 to −3 °C that provides additional support for the assignment of their EPR spectrum to $[S_4N_4]^{-\bullet}$.

Exhaustive polarographic[3d−3f] and coulometric[3e,9] studies on S_4N_4 have confirmed the initial one-electron reduction process at room temperature. The final products of reduction in aprotic solvents are salts of $[S_3N_3]^-$ that appear to be produced quantitatively with the uptake of 1.3 e^- per S_4N_4. Coulometric reduction in the presence of proton donors (acetic or monochloroacetic acids) yields the tetraimide $S_4N_4H_4$.[3d] The electrochemical oxidation of $[S_3N_3]^-$ (as the Et_4N^+ salt in $CH_3CN/[Et_4N][ClO_4]$) produces S_4N_4 almost quantitatively;[3e] however, attempts to detect a radical upon electrolytic oxidation of $[PPN][S_3N_3]$ in CH_2Cl_2 by EPR spectroscopy were unsuccessful.[10] Very recently the photochemistry of S_4N_4 was investigated in Ar matrixes, demonstrating the facile interconversion of S_4N_4 to different isomers.[11] Three intermediates were identified with the aid of DFT calculations, two of which are novel S_3N_3 rings carrying exocyclic (N)−S≡N or (S)−N═S groups. These two bear a strong resemblance to species postulated in this work for the decay of $[S_4N_4]^{-\bullet}$ and may be directly involved in the coupling of neutral $[NS]^\bullet$ with $[S_3N_3]^\bullet$.

We recently reported[12] the first identification of the radical anions of unsaturated $C_2N_4S_2$ (**3**) and $P_2N_4S_2$ (**4**) rings by using an in situ electrochemical cell capable of Simultaneous Electrochemical Electron Paramagnetic Resonance (SEEPR)[13] spectroscopy, as well as an investigation of the mechanism of their decomposition by a kinetic analysis employing modern digital simulation of CVs. In connection with our interest in the characterization of short-lived, binary S,N radicals,[14] we now report the application of these methods to detailed investigations of (a) the reduction of S_4N_4 and (b) the oxidation of $[S_3N_3]^-$. In part (a) we have used the SEEPR technique to acquire high quality EPR spectra of the anion radical $[S_4N_4]^{-\bullet}$ using natural abundance, ^{15}N and ^{33}S-enriched S_4N_4 at low temperature. We have also employed digital simulations of CVs to provide insights into the nature of the $S_4N_4 \leftrightarrow [S_3N_3]^-$ interconversion. The target of part (b) was $[S_3N_3]^\bullet$ in condensed phases; this radical has previously only been detected in the vapors of $(SN)_x$ by photoelectron spectroscopy.[15] The $[S_3N_3]^\bullet$ radical has also been invoked as an intermediate in the formation of $[S_3N_3]^-$ salts from the ten-membered ring $[S_5N_5]Cl$ via ring contraction.[16a] Interestingly, the compound $[PhCN_2S_2][S_3N_3]$, which can be obtained by the reaction of the dimer $(PhCN_2S_2)_2$ with the vapors formed from $(SN)_x$ at 160 °C, is described as a biradical $[PhCN_2S_2]^\bullet[S_3N_3]^\bullet$ rather than an ionic compound on the basis of ab initio molecular orbital calculations.[16a] However, single-crystal EPR studies could detect only ∼1% $[PhCN_2S_2]^\bullet$ trapped in a matrix of what seems to be $[PhCN_2S_2]^+[S_3N_3]^-$.[16b] Surprisingly, despite the apparent solubility of this adduct in common solvents, no solution-phase EPR evidence which could corroborate the biradical nature of this compound was reported. In pursuit of the elusive $[S_3N_3]^\bullet$ radical we have carried out a detailed CV and SEEPR study of the oxidation of the $[S_3N_3]^-$ anion in the form of the known $[Cp_2Co]^+$ and $[PPN]^+$ (PPN = $[(Ph_3P)_2N]^+$) salts.[4d,17] The X-ray structure of the $[PPN]^+$

(6) Gillespie, R. J.; Kent, J. P.; Sawyer, J. F.; Slim, D. R.; Tyrer, J. D. *Inorg. Chem.* **1981**, *20*, 3799–3812.
(7) (a) Chandra, H.; Rao, D. N. R.; Symons, M. C. R. *J. Chem. Soc., Dalton Trans.* **1987**, 729–732. (b) Müller, U.; Conradi, E.; Demant, U.; Dehnicke, K. *Angew. Chem., Int. Ed.* **1984**, *23*, 237–238.
(8) Cordes, A. W.; Marcellus, C. G.; Noble, M. C.; Oakley, R. T.; Pennington, W. T. *J. Am. Chem. Soc.* **1983**, *105*, 6008–6012.
(9) Brown, O. R. *J. Electroanal. Chem.* **1972**, *34*, 419–423.
(10) Fritz, H. P.; Bruchhaus, R.; Mews, R.; Höfs, H.-U. *Z. Anorg. Allg. Chem.* **1985**, *525*, 214–220.
(11) Pritchina, E. A.; Gritsan, N. P.; Zibarev, A. V.; Bally, T. *Inorg. Chem.* **2009**, *48*, 4075–4088.
(12) Boeré, R. T.; Bond, A. M.; Chivers, T.; Feldberg, S. W.; Roemmele, T. L. *Inorg. Chem.* **2007**, *46*, 5596–5607.
(13) (a) Webster, R. D.; Bond, A. M.; Coles, B. A.; Compton, R. G. *J. Electroanal. Chem.* **1996**, *404*, 303–308. (b) Fiedler, D. A.; Koppenol, M.; Bond, A. M. *J. Electrochem. Soc.* **1995**, *142*, 862–867. (c) Neudeck, A.; Kress, L. *J. Electroanal. Chem.* **1997**, *437*, 141–156.
(14) Boeré, R. T.; Tuononen, H. M.; Chivers, T.; Roemmele, T. L. *J. Organomet. Chem.* **2007**, *692*, 2683–2696.
(15) (a) Lau, W. M.; Westwood, N. P. C.; Palmer, M. H. *J. Chem. Soc., Chem. Commun.* **1985**, 752–753. (b) Lau, W. M.; Westwood, N. P. C.; Palmer, M. H. *J. Am. Chem. Soc.* **1986**, *108*, 3229–3237.
(16) (a) Banister, A. J.; Hansford, M. I.; Hauptman, Z. V.; Luke, A. W.; Wait, S. T.; Clegg, W.; Jorgensen, K. A. *J. Chem. Soc., Dalton Trans.* **1990**, 2793–2802. (b) Lee, F. L.; Preston, K. F.; Williams, A. J.; Sutcliffe, L. H.; Banister, A. J.; Wait, S. T. *Magn. Reson. Chem.* **1989**, *27*, 1161–1165.
(17) Jagg, P. N.; Kelly, P. F.; Rzepa, H. S.; Williams, D. J.; Woollins, J. D.; Wylie, W. *J. Chem. Soc., Chem. Commun.* **1991**, 942–944.

salt is also described. These experimental investigations are supplemented by high-level theoretical calculations of the electronic structure of $[S_3N_3]^{\bullet}$.

Experimental Section

Reagents and General Procedures. S_4N_4,[3k,3l] as well as the ^{15}N and ^{33}S isotope-labeled analogues,[18] $[Cp_2Co][S_3N_3]$[17] and $[PPN][S_3N_3]$[4d,4e,19] were obtained by literature methods. The isotopic purity of 99.9% $^{33}S_4{}^{14}N_4$ was confirmed using LRMS: 187.9 ($^{33}S_4{}^{14}N_4{}^+$, 2%); 140.9 ($^{33}S_3{}^{14}N_3{}^+$, 13%); 93.9 ($^{33}S_2{}^{14}N_2{}^+$, 19%); 47.0 ($^{33}S^{14}N^+$, 100%). Dichloromethane and acetonitrile (BDH, reagent grade) were purified by distillation (CH_3CN: first from P_2O_5, then CaH_2, CH_2Cl_2: from CaH_2). Both solvents were purged with dry nitrogen prior to use. Electrochemical grade tetrabutylammonium hexafluorophosphate $[^nBu_4N][PF_6]$ (Fluka) was used as the supporting electrolyte and was stored in a desiccator. Ferrocene (Fc) was sublimed prior to use.

Voltammetry. Cyclic voltammograms were obtained at 21 ± 2 °C in both CH_3CN and CH_2Cl_2 solutions containing 0.1 and 0.4 M $[^nBu_4N][PF_6]$, respectively, as the supporting electrolyte. These solutions were purged with dry nitrogen for 10 min directly before use, and were kept under a blanket of nitrogen during all experiments. CVs, bulk electrolysis, and rotating disk electrode (RDE) measurements were performed with a Princeton Applied Research PARSTAT 2273 potentiostat in conjunction with a PINE Model AFMSRXE Modulated Speed Rotator. The voltammetry cell design has been described previously.[12] The cell used for RDE measurements replaced the central size-10 joint with a 60 × 15 mm cylinder to accommodate the rotating electrode. Initial background scans characterized the size of the accessible electrochemical window and provided an estimate of the likely background current. The CVs were obtained over scan rates of 0.05−20 V s^{-1}. The potentials for S_4N_4 and $[PPN][S_3N_3]$ are reported versus the operative formal potential, $E^0_{Fc^{0/+}}$, for the Fc/Fc^+ redox couple, which was used as an internal standard. Potentials for $[Cp_2Co][S_3N_3]$ are also quoted versus ferrocene, for which the cobaltocene/cobaltocenium redox couple is known to appear at −1.35 V in dichloromethane.[20] The 3.0 mm BASi glassy carbon (GC) working electrode area (6.6×10^{-2} cm^2) was determined from the peak current value obtained for the reversible one-electron reduction of ferrocene (1.0 mM, 2.0 mM, and 3.0 mM solutions) in CH_3CN (0.1 M $[^nBu_4N][PF_6]$) under conditions of CV and using the Randles−Sevcik equation:[21]

$$I_p = 0.4463nF\left(\frac{nF}{RT}\right)^{1/2} AD^{1/2}\nu^{1/2}C \qquad (1)$$

where I_p is the peak current (A), n (the number of electrons in the charge-transfer process) is taken to be 1.0, A is the electrode area (cm^2), D is the diffusion coefficient (taken to be 2.3×10^{-5} cm^2 s^{-1}),[21] C is the concentration (mol cm^{-3}), ν is the scan rate (V s^{-1}), and the other symbols have their usual meanings. The working electrode was polished with an Al_2O_3 (Buehler, 0.05 μm) slurry on a clean polishing cloth, rinsed with distilled water, and dried with tissue paper prior to use. A 5.0 mm diameter GC macrodisk electrode (area = 1.86×10^{-1} cm^2) obtained from Pine Instruments was employed for RDE voltammetry. Diffusion coefficients were determined from limiting current values obtained from RDE voltammetry and use of the Levich equation:[21]

$$I_l = 0.62nFAD_o^{2/3}\omega^{1/2}\nu_k{}^{-1/6}C_o^* \qquad (2)$$

where I_l is the limiting current, ω is the angular frequency of rotation (s^{-1}), (ν_k) is the kinematic viscosity, and the other symbols have been described above. Values for kinematic viscosity at 20 °C were taken to be those for the pure solvents: 0.004536 cm^2 s^{-1} for CH_3CN[22] and 0.003318 cm^2 s^{-1} for CH_2Cl_2.[22] The almost linear plots of $I_p{}^{c1}$ versus $\nu^{1/2}$ obtained for the first reduction process in S_4N_4, as well as of $I_p{}^{a2}$ versus $\nu^{1/2}$ for the first oxidation process in $[S_3N_3]^-$ in CH_2Cl_2 at a GC working electrode implies that the mass transport process at the peak potential is controlled by diffusion in both cases. From the Randles−Sevcik relationship (eq 1) an estimation of the diffusion coefficients was also obtained from straight line fits to the $I_p{}^{c1}$ versus $\nu^{1/2}$ and $I_p{}^{a2}$ versus $\nu^{1/2}$ plots, respectively.

Simulations of CV Responses for S_4N_4 and $[S_3N_3]^-$. Theoretical cyclic voltammograms were simulated with the DigiElch simulation package (www.elchsoft.com). The simulation algorithm used in this program has been described previously.[23] Values for the ohmic resistance (R_u) were determined by measuring the impedance of the system at potentials where the Faradaic current was negligibly small. Unless otherwise stated, the charge-transfer coefficients were assumed to be 0.5, and the average values for the diffusion coefficients of S_4N_4 and $[S_3N_3]^-$ were taken to be 1.17×10^{-5} cm^2 s^{-1} and 4.00×10^{-6} cm^2 s^{-1}, respectively.

Bulk Electrolysis and ex situ EPR Experiments. Bulk electrolysis was performed by using a cylindrical platinum electrode, a planar platinum mesh auxiliary electrode, and a silver wire quasi-reference electrode, both separated from the solution by 1.0−1.6 μm porosity frits, in a previously described cell.[24] Ex situ EPR experiments were conducted on a solution of $[Cp_2Co][S_3N_3]$ in CH_2Cl_2 at 0 °C. Oxidative electrolysis at −0.2 V (vs Fc/Fc^+) was commenced and after approximately 1 min, a 1 mL aliquot of the oxidized solution was taken and injected into a 4 mm (o.d.) quartz EPR tube which had been previously vacuum purged and backfilled with N_2(g). The tube was immediately capped and inserted into liquid nitrogen. This procedure was repeated three more times at 1 min intervals, and the four samples were taken and inserted into the EPR cavity held at −153 °C.

SEEPR Experiments. SEEPR experiments were conducted on solutions of S_4N_4, $[Cp_2Co][S_3N_3]$, and $[PPN][S_3N_3]$ in $CH_2Cl_2/[^nBu_4N][PF_6]$ at temperatures between −80 and +30 °C, as well on 99% ^{15}N-enriched and 99.92% enriched ^{33}S labeled S_4N_4. The room temperature studies were conducted with a Wilmad quartz electrolytic flat cell with a laminated gold-micromesh working electrode described previously.[12] Low-temperature studies employed a miniature quartz flat cell (Wilmad WG-808) incorporating modified electrodes which are all fed in from the top of the cell and therefore fits inside the standard Bruker N_2 Dewar insert. The Bruker EMX 113 spectrometer was operated at X-band frequencies (9.8 GHz) and spectra were monitored in intensity-versus-field mode during electrolysis, as well as in intensity-versus-time mode after electrolysis was terminated. Plots of $\ln(C_t/C_{t=0})$ versus t (where C = signal intensity, t = time in seconds) as well as of $1/(C_t/C_{t=0})$ versus

(18) (a) Lipp, S. A.; Chang, J. J.; Jolly, W. M. *Inorg. Chem.* **1970**, *9*, 1970–1973. (b) Jolly, W. L.; Maguire, K. D. *Inorg. Synth.* **1969**, *9*, 102–111.
(19) (a) Ruff, J. K.; Schlientz, W. J. *Inorg. Synth.* **1974**, *15*, 84–87. (b) Blohm, M. L.; Gladfelter, W. L. *Inorg. Synth.* **1989**, *26*, 286–289.
(20) Stojanovic, R. S.; Bond, A. M. *Anal. Chem.* **1993**, *65*, 56–64.
(21) Bard, A. J.; Faulkner, L. R. *Electrochemical Methods: Fundamentals and Applications*, 2nd ed.; Wiley: New York, 2001.
(22) Lide, D. R., *CRC Handbook of Chemistry and Physics*, 85th ed.; CRC Press: Boca Raton, 2004; Section 6, p 203ff. See alsoNath, J.; Dixit, A. P. *J. Chem. Eng. Data* **1984**, *29*, 317–319. and Adam, H. H.; Baignie, B. D.; Joslin, T. A. *J. Chem. Soc., Perkin Trans. 2* **1977**, 1287–1293.
(23) (a) Rudolph, M. *J. Electroanal. Chem.* **2003**, *543*, 23–39. (b) Rudolph, M. J. *J. Electroanal. Chem.* **2004**, *571*, 289–307. (c) Rudolph, M. *J. Electroanal. Chem.* **2003**, *558*, 171–176. (d) Rudolph, M. *J. Comput. Chem.* **2005**, *26*, 619–632. (e) Rudolph, M. *J. Comput. Chem.* **2005**, *26*, 1193–1204.
(24) Bond, A. M. *Broadening Electrochemical Horizons*; Oxford University Press: New York, 2002.

t were used to determine the rate of decay of the radicals. Simulations of EPR spectra were performed with Bruker Simfonia (version 1.25) and WinSim (version 0.98, 2002) software.[25] Experimental *g* values were determined with reference to external, solid DPPH (2.0037 ± 0.0002).[26] Spectral parameters for $[S_4N_4]^{-\bullet}$ in CH_2Cl_2: conversion times (CT) = 40.96 or 81.92 s, sweep width (SW) = 6.0 mT, modulation amplitude (MA) = 0.05 mT; for ^{15}N labeled $[S_4N_4]^{-\bullet}$ in CH_2Cl_2: CT = 40.96 or 81.92 s, SW = 6.0 mT, MA = 0.05 mT; for ^{33}S labeled $[S_4N_4]^{-\bullet}$ in CH_2Cl_2: CT = 40.96 or 81.92 s, SW = 12.0 mT, MA = 0.1 mT. The temperature inside the EPR cavity was calibrated using a Copper-Constantan Thermocouple which was previously calibrated using both ice/water and dry ice/CH_3OH baths. The temperatures were recorded at 10° intervals against the VT controller over the range of −89 to +19.5 °C.

Crystallography. A small block of [PPN][S_3N_3] cut from a longer pale-green needle was mounted on a glass capillary using Paratone oil and cooled to −173(2) °C. The ambiguous space group choice between *Cc* and *C*2/*c* was investigated by solving the structure in both space groups. Full details are provided in the Supporting Information as well as in the electronic CIF file.[27] These data can be obtained free of charge from the Cambridge Crystallographic Data Centre via www.ccdc.cam.ac.uk/products/csd/request/request.php4.

Computational Details. Theoretical calculations were carried out for the $[S_3N_3]^{\bullet}$ radical using Hartree−Fock (HF), Möller-Plesset perturbation theory (MP2),[28] coupled cluster (CCSD)[29] and complete active space (CAS) methods,[30] Dunning's correlation consistent basis set of triple-ζ quality, cc-pVTZ, was used for all atoms.[31] The CAS calculations utilized a minimum active space consisting of three orbitals and three electrons, that is, [3,3]-CAS. Harmonic vibrational frequencies were calculated for all optimized geometries. Software used included Gaussian 03,[32] Molpro 2002.6,[33] and gOpenMol.[34]

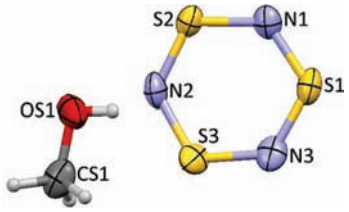

Figure 1. Thermal ellipsoid plot (Mercury 2.2, CCDC, 2008) showing the anion and hydrogen-bonded CH_3OH molecule as determined in the crystal structure of [PPN][$S_3N_3 \cdot HOCH_3$].

Table 1. Diffusion Coefficient Values for S_4N_4 and $[S_3N_3]^-$ in CH_2Cl_2[a]

electrode	RPM	D (S_4N_4)/10^{-5} cm^2 s^{-1}	D ($[S_3N_3]^-$)/10^{-5} cm^2 s^{-1}
		RDE[a]	
GC	2250	1.20[b]	0.406[c]
GC	2000	1.20[b]	0.408[c]
GC	1750	1.20[b]	0.408[c]
GC	1500	1.20[b]	0.406[c]
GC	1250	1.21[b]	0.408[c]
GC	1000	1.22[b]	0.408[c]
		RDE (Koutecky−Levich)[d]	
GC		1.26[b]	0.411[c]
GC		1.11[e]	0.402[f]
		CV[d]	
GC		0.96[g]	0.34[h]

[a] T = 21 ± 2 °C 0.4 M [^{n}Bu$_4$N][PF$_6$], ν = 0.01 V s^{-1}. [b] 3.88 mM. [c] 1.29 mM [Cp$_2$Co][S_3N_3]. [d] 0.4 M [^{n}Bu$_4$N][PF$_6$],], ν = 0.1−0.5 V s^{-1}. [e] 2.21 mM. [f] 2.08 mM [Cp$_2$Co][S_3N_3]. [g] 1.05 mM. [h] 1.30 mM [Cp$_2$Co][S_3N_3].

Table 2. Selected Bond Lengths [Å] and Angles [deg] for [PPN][$S_3N_3 \cdot HOCH_3$]

N(1)−S(1)	1.615(5)	S(1)−N(1)−S(2)	123.8(3)
N(1)−S(2)	1.630(5)	S(2)−N(2)−S(3)	124.2(3)
N(2)−S(2)	1.616(6)	S(1)−N(3)−S(3)	123.2(4)
N(2)−S(3)	1.646(5)	N(3)−S(1)−N(1)	117.5(3)
N(3)−S(1)	1.605(6)	N(2)−S(2)−N(1)	115.4(3)
N(3)−S(3)	1.632(6)	N(3)−S(3)−N(2)	115.5(3)
N(4)−P(2)	1.577(4)	P(2)−N(4)−P(1)	136.1(2)
N(4)−P(1)	1.593(4)	N(4)−P(1)−C(1)	111.4(2)

Results and Discussion

Characterization of [PPN][$S_3N_3 \cdot HOCH_3$]. Of the known salts of $[S_3N_3]^-$[4,16,17,35] there are five reported crystal structures, for which the cations are [^{n}Bu$_4$N],[4g] [(PhCN$_2$S$_2$)$_2$Cl],[35] [PhCN$_2$S$_2$],[16a] [PPh$_4$],[4f] and [CoCp$_2$].[17] Here we report the structure of [PPN][S_3N_3] obtained on lime-green crystals from CH_2Cl_2/CH_3OH.[36] The anion and solvent are shown in Figure 1, and the asymmetric unit including $[PPN]^+$ is provided in the Supporting Information, Figure S1. Selected bond lengths and angles for this compound are listed in Table 2. The average

(25) Duling, D. R. *J. Magn. Reson., Ser. B* **1994**, *104*, 105–110.
(26) Weil, J. A.; Bolton, J. R.; Wertz, J. E. *Electron Paramagnetic Resonance*; John Wiley & Sons: New York, 1994.
(27) Crystal data for [PPN][$S_3N_3 \cdot HOCH_3$]: $C_{37}H_{34}N_4OP_2S_3$, M_r = 708.80, monoclinic space group *Cc*, a = 15.5470(8), b = 15.9857(8), c = 14.6976(7) Å, β = 109.363(1)°, V = 3446.2(3) Å^3, Z = 4, T = 100(2) K, ρ_{calcd} = 1.366 g/cm^3, μ(Mo Kα) = 0.345 mm^{-1}, 22701 reflections collected (Θ range = 1.88−26.37°), 3521, unique (R_{int} = 0.0411), R_1 = 0.0421 [for 3241 reflections with $I > 2\sigma(I)$] and wR_2 = 0.1118 (for all data); GOF on F^2 = 1.062, completeness = 1.000.
(28) Møller, C.; Plesset, M. S. *Phys. Rev.* **1934**, *46*, 618–622.
(29) See, for example: Bartlett, R. J. *J. Phys. Chem.* **1989**, *93*, 1697–1708, and references therein.
(30) Roos., B. O.; Taylor, P. R.; Siegbahn, P. E. M. *Chem. Phys.* **1980**, *48*, 157–173.
(31) (a) Dunning, T. H. Jr., *J. Chem. Phys.* **1989**, *90*, 1007–1023. (b) Woon, D. E.; Dunning, T. H. Jr., *J. Chem. Phys.* **1993**, *98*, 1358–1371.
(32) Frisch, M. J.; Trucks, G. W.; Schlegel, H. B.; Scuseria, G. E.; Robb, M. A.; Cheeseman, J. R.; Montgomery, Jr., J. A.; Vreven, T.; Kudin, K. N.; Burant, J. C.; Millam, J. M.; Iyengar, S. S.; Tomasi, J.; Barone, V.; Mennucci, B.; Cossi, M.; Scalmani, G.; Rega, N.; Petersson, G. A.; Nakatsuji, H.; Hada, M.; Ehara, M.; Toyota, K.; Fukuda, R.; Hasegawa, J.; Ishida, M.; Nakajima, T.; Honda, Y.; Kitao, O.; Nakai, H.; Klene, M.; Li, X.; Knox, J. E.; Hratchian, H. P.; Cross, J. B.; Bakken, V.; Adamo, C.; Jaramillo, J.; Gomperts, R.; Stratmann, R. E.; Yazyev, O.; Austin, A. J.; Cammi, R.; Pomelli, C.; Ochterski, J. W.; Ayala, P. Y.; Morokuma, K.; Voth, G. A.; Salvador, P.; Dannenberg, J. J.; Zakrzewski, V. G.; Dapprich, S.; Daniels, A. D.; Strain, M. C.; Farkas, O.; Malick, D. K.; Rabuck, A. D.; Raghavachari, K.; Foresman, J. B.; Ortiz, J. V.; Cui, Q.; Baboul, A. G.; Clifford, S.; Cioslowski, J.; Stefanov, B. B.; Liu, G.; Liashenko, A.; Piskorz, P.; Komaromi, I.; Martin, R. L.; Fox, D. J.; Keith, T.; Al-Laham, M. A.; Peng, C. Y.; Nanayakkara, A.; Challacombe, M.; Gill, P. M. W.; Johnson, B.; Chen, W.; Wong, M. W.; Gonzalez, C.; and Pople, J. A.; *Gaussian 03*, Revision C.02; Gaussian, Inc.: Wallingford, CT, 2004.
(33) Molpro 2002.6 is a package of ab initio programs designed by H.-J. Werner and P. J. Knowles. The authors are Amos, R. D.; Bernhardsson, A.; Berning, A.; Celani, P.; Cooper, D. L.; Deegan, M. J. O.; Dobbyn, A. J.; Eckert, F.; Hampel, C.; Hetzer, G.; Knowles, P. J.; Korona, T.; Lindh, R.; Lloyd, A. W.; McNicholas, S. J.; Manby, F. R.; Meyer, W.; Mura, M. E.; Nicklass, A.; Palmieri, P.; Pitzer, R.; Rauhut, G.; Schütz, M.; Schumann, U.; Stoll, H.; Stone A. J.; Tarroni, R.; Thorsteinsson, T.; Werner, H.-J.
(34) (a) Laaksonen, L. *J. Mol. Graph.* **1992**, *10*, 33–34. (b) Bergman, D. L.; Laaksonen, L.; Laaksonen, A. *J. Mol. Graph. Model.* **1997**, *15*, 301–306.
(35) Banister, A. J.; Clegg, W.; Hauptman, Z. V.; Luke, A. W.; Wait, S. T. *J. Chem. Soc., Chem. Commun.* **1989**, 351–352.
(36) The published synthesis of [PPN][S_3N_3] mentions recrystallization of the salt using identical solvents and conditions, but there is no mention of a solvent adduct (ref 4d).

Table 3. CV Data Obtained for S_4N_4, $[Cp_2Co][S_3N_3]$, and $[PPN][S_3N_3]$ in CH_2Cl_2[a]

cmpd	conc (mM)	E_p^{a1} (V)	E_p^{c1} (V)	E_m[b] (V)	E_p^{a2} (V)	E_p^{c2} (V)	E_n[c] (V)
S_4N_4	3.90	−0.93	−1.06	−1.00	−0.29	−0.36	−0.33
$[Cp_2Co][S_3N_3]$[d]	2.16		−1.03		−0.30	−0.38	−0.34
$[PPN][S_3N_3]$	3.90	−0.95	−1.04	−1.00	−0.31	−0.37	−0.34

[a] Obtained at a GC electrode at $\nu = 0.2$ V s^{-1} and $T = 21 \pm 1$ °C. [b] $E_m = [E_p^{a1} + E_p^{c1}]/2 \approx E^{o/}_{(1)}$. [c] $E_n = [E_p^{a2} + E_p^{c2}]/2 \approx E^{o/}_{(2)}$. [d] $E^{o/}_{(3)} = [E_p^{a3} + E_p^{c3}]/2 = -1.35$ V, ($E_p^{a3} - E_p^{c3} = 100$ mV).

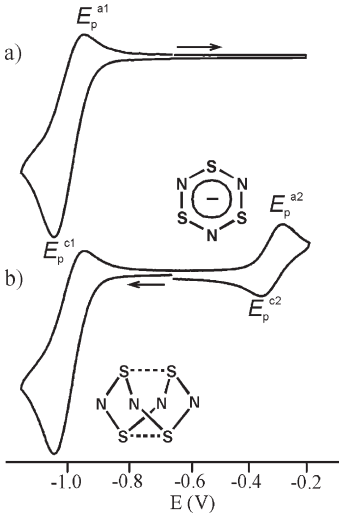

Figure 2. CVs over an extended potential window obtained on 3.90 mM solutions of S_4N_4 in CH_2Cl_2 containing 0.4 M [^{n}Bu$_4$N][PF$_6$] at a GC electrode at 21.5 °C, $\nu = 0.2$ V s^{-1} with the potential starting at −0.65 V: (a) sweeping in the positive direction and (b) sweeping in the negative direction.

S−N bond lengths and angles from the five previously reported salts are: S−N = 1.607(21) Å; ∠SNS = 123.8(10)°; ∠NSN = 116.1(9)° (all data were collected at 22 °C). The S−N distances and angles are not significantly different in $[PPN][S_3N_3]$ because of the wide range observed in known structures. $[S_3N_3]^-$ is found to be almost planar in the crystal lattice (mean rms deviation below 2.6%, less than observed for any of the six phenyl rings in the cation) but the bond distances and angles do appear distorted as a consequence of the H-bonding interaction with the methanol solvate molecule, with the longest bond and angle adjacent to H. However, the large published variation in these parameters in previous structures leaves this assignment inconclusive. The H-bond between MeOH and the N(2) nitrogen atom is quite typical with a length of 2.829 Å and a bond angle of 162.3°.

Voltammetry. S_4N_4, $[Cp_2Co][S_3N_3]$, and $[PPN][S_3N_3]$ were studied by CV in CH_2Cl_2 over scan rates of 0.05−20 V s^{-1} and temperatures of 21 ± 2 °C. Voltammetric results for S_4N_4, $[Cp_2Co][S_3N_3]$, and $[PPN][S_3N_3]$ in CH_2Cl_2 are reported in Table 3. Representative CVs obtained from solutions of S_4N_4 at a scan rate of 0.2 V s^{-1} are shown in Figure 2. CVs of the initial reduction process of S_4N_4 within a narrow potential window displayed a small return wave at moderate-to-slow scan rates, which increased in peak current height with increasing scan rate. A close-to-linear scaling of the Faradaic current was observed with concentration of S_4N_4 in CH_2Cl_2

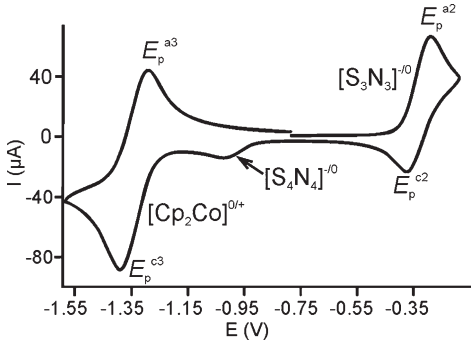

Figure 3. CV obtained on 2.16 mM solutions of $[Cp_2Co][S_3N_3]$ in CH_2Cl_2 at a GC electrode at 22 °C, 0.4 M [^{n}Bu$_4$N][PF$_6$], $\nu = 0.2$ V s^{-1}.

(Supporting Information, Table S2), implying that the influence of uncompensated resistance was minimal under our high supporting electrolyte (0.4 M [^{n}Bu$_4$N][PF$_6$]) conditions. Coulometric measurements (vide infra) indicate that the overall process involves the transfer of approximately 1.3 electrons per S_4N_4 molecule; this strongly suggests an initial one-electron reduction process followed by recycling of "NS". A second, irreversible reduction process occurs at approximately −1.6 V versus Fc/Fc^+ which has not been explored further.

CVs obtained over an electrochemical window that was extended considerably in the anodic direction show the absence (Figure 2a) of secondary processes when the initial sweep direction is anodic, but the presence (Figure 2b) of a new redox couple at $E_n = -0.33$ V versus Fc/Fc^+ when the potential is first swept through the reduction process. This indicates that the new process involves a species generated from the decomposition of $[S_4N_4]^{-\bullet}$. On the basis of prior investigations (vide supra), the new process is attributed to the $[S_3N_3]^{-/0}$ redox couple. Williford et al. claimed to have seen several products oxidizable at potentials more positive than the reduction of S_4N_4 in $CH_3CN/[Et_4N][ClO_4]$ at room temperature (RT) but did not report any details on these processes.[3c]

We have therefore investigated both $[PPN][S_3N_3]$ and $[Cp_2Co][S_3N_3]$ by CV under identical conditions to those employed for solutions of S_4N_4. CVs of $[PPN][S_3N_3]$ in CH_2Cl_2 clearly show $[S_3N_3]^{-/0}$ at $E_n = -0.34$ V versus Fc/Fc^+[37] but the absence of any further redox couples up to the solvent limit when the scan is first swept in the cathodic direction. Once the potential is swept anodically over potentials including the $[S_3N_3]^{-/0}$ redox couple and the sweep direction is reversed, a new redox couple appears at −1.00 V. CVs of $[Cp_2Co][S_3N_3]$ in CH_2Cl_2 also show the $[S_3N_3]^{-/0}$ redox couple at $E_n = -0.34$ V, and another couple at $E^{o/} = -1.35$ V, attributable to $[Cp_2Co]^{0/+}$, with a shoulder at −1.03 V (Figure 3). The appearance of these secondary features with comparable E_p^{c1} values to those of S_4N_4 subsequent to cycling the potentials through $[S_3N_3]^{-/0}$ indicates rapid generation of S_4N_4, presumably from decay of neutral $[S_3N_3]^{\bullet}$. A third reduction process occurs at about −2.30 V in $[Cp_2Co][S_3N_3]$, which is readily attributed to the

(37) This redox couple was previously reported from $[PPN][S_3N_3]$ in CH_2Cl_2/[^{n}Bu$_4$N][BF$_4$] to be "reversible" and to occur at +0.17 V vs SCE (−0.31 V vs Fc^+/Fc) in the same solvent (ref 10). This difference in standard potential can be accounted for by differences in interfacial potentials from the use of the SCE reference electrode.

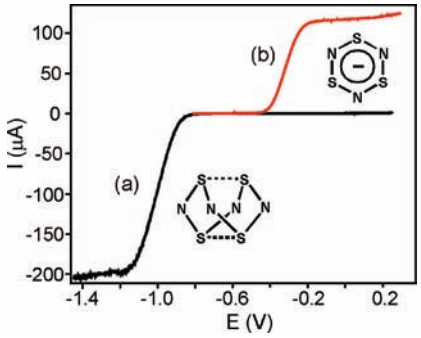

Figure 4. RDE voltammograms obtained on a 1.29 mM solution of S_4N_4 at a 5 mm GC electrode rotating at 500 rpm, $\nu = 0.01$ V s^{-1} at 0 °C, showing (a) potential sweep from +0.25 to −1.45 V (black line) before electrolysis, and (b) potential sweep from −0.9 V to +0.25 V after exhaustive electrolysis at −1.25 V (red line).

$[Cp_2Co]^{-/0}$ redox couple.[20] A second, irreversible oxidation peak is also seen at +0.72 V which has a much smaller peak current height when compared to $[S_3N_3]^{-/0}$. No other redox couples appeared within the solvent window (−2.3 to +1.6 V).

The $[S_3N_3]^{-/0}$ redox couple displayed sizable return waves at moderate scan rates (0.1−0.5 V s^{-1}) and temperatures of 21 ± 2 °C, with I_p^{c2}/I_p^{a2} values between = 0.62−0.69 which are similar to those observed from $[S_3N_3]^-$ generated from bulk S_4N_4 solution (Figure 2). However, the peak currents of the $[S_3N_3]^{-/0}$ and $[Cp_2Co]^{0/+}$ processes were consistently observed to be uneven ($I_p^{a2}/I_p^{c3} \sim 0.56-0.57$), despite the fact that the two species were present in identical concentration in view of their common source in one salt (Figure 3).

The peak current of a CV wave under Nernstian conditions is given by eq 1.[21] Thus, $I_p \propto (D_0)^{1/2}$ and estimates for the diffusion coefficient of $[Cp_2Co]^+$ ions are 1.66×10^{-5} cm^2 s^{-1} in $CH_2Cl_2/[^nBu_4N][PF_6]$[38] and 1.7×10^{-5} cm^2 s^{-1} in CH_2Cl_2 alone (by NMR methods).[39] The use of these values and the average diffusion coefficient of $[S_3N_3]^-$ from this study (see Table 1) predicts a current ratio of about 0.49, which is in reasonable agreement with that observed in the CVs. Hence, we attribute the unusually small peak currents for the oxidation of $[S_3N_3]^-$ to the anomalously small diffusion coefficient of this ion in CH_2Cl_2. A close-to-linear scaling of the Faradaic current was observed with concentration of $[S_3N_3]^-$ in CH_2Cl_2 (Supporting Information, Table S3), implying that the influence of uncompensated resistance was minimal at this concentration of supporting electrolyte (0.4 M $[^nBu_4N][PF_6]$).

Bulk Electrolysis of S_4N_4. The conversion of S_4N_4 to $[S_3N_3]^-$ has been claimed to be almost quantitative via exhaustive electrolysis of S_4N_4 at potentials corresponding to the first reduction process in both CH_3CN[3e] and anhydrous ethanol.[4a,4b] We undertook to check the validity of such a conversion in CH_2Cl_2, the solvent used in this study, and have monitored the electrolysis both by coulometry and by RDE voltammograms taken before and after the completion of electrolysis (Figure 4). Electrolysis of 1.29 mM solutions of S_4N_4 in CH_2Cl_2/(0.1 M $[^nBu_4N][PF_6]$) at −1.25 V (vs Fc/Fc^+) for 41 min led to the disappearance of the wave for S_4N_4, and the growth of a new wave corresponding to the half-wave potential for oxidation of $[S_3N_3]^-$. Quantitative conversion is indicated both by the value of n, the number of electrons transferred (1.3 per S_4N_4), from coulometry and the size of the RDE currents. The much larger current for S_4N_4 (at 3/4 the concentration of $[S_3N_3]^-$) should be placed in the context of the large difference in diffusion coefficients for the two species. Using the ratio of the 200 and 118 μA limiting currents to the average D_0 values and the 4:3 stoichiometry ratio, the RDE voltammograms indicate essentially complete conversion (~97%), in good agreement with the value from coulometry.

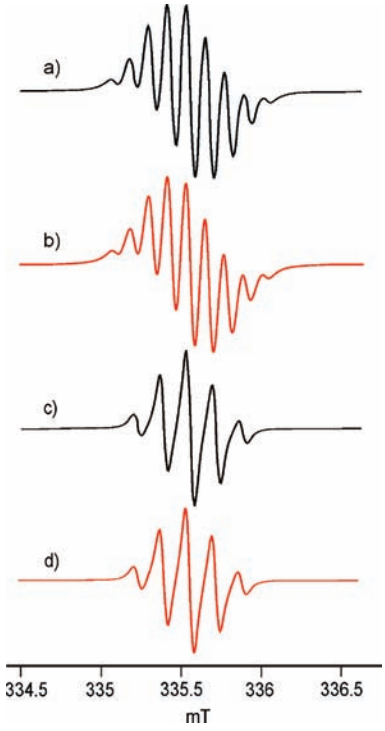

Figure 5. (a) Experimental (black line) and (b) simulated (red line) first derivative EPR spectra obtained during in situ reductive electrolysis (82 s single scan) of a 3.1 mM solution S_4N_4 at a gold micromesh electrode at −20 °C in CH_2Cl_2 (0.4 M $[^nBu_4N][PF_6]$): modulation amplitude = 0.05 mT. (c) Experimental (black line) and (d) simulated (red line) spectra obtained in similar manner from a 1.2 mM solution of 99% enriched $^{32}S_4{}^{15}N_4$ at a gold micromesh electrode at −10 °C in CH_2Cl_2 (0.4 M $[^nBu_4N][PF_6]$): modulation amplitude = 0.05 mT. g value = 2.0008(1).

SEEPR Experiments: EPR Spectra of $[S_4N_4]^{-\bullet}$. Utilization of a conventional aqueous flat cell with a very large surface-area working electrode allowed observation of a nine-line spectrum (Supporting Information, Figure S2) after single 82 s scans at RT. This spectrum was recognizably the same as that reported previously at temperatures below 0 °C,[3b,3c] but with excessively broadened lines (line width, LW, = 0.135 mT, a(N) = 0.117 mT). By switching to a smaller low-temperature SEEPR cell, high quality EPR spectra from single 41 or 82 s scans were obtained upon reductive electrolysis at −1.10 V at 0 °C or lower (Figures 5,6). With natural-abundance S_4N_4, the expected nine-line pattern can be simulated using four equivalent $a(^{14}N)$ = 0.1175 mT, LW = 0.06 mT, and g value = 2.0008(1), in good agreement with the literature values (Table 4).[3b,3c] Spectra obtained at temperatures between −80 to 0 °C are of similar quality with little

(38) Cooper, J. B.; Bond, A. M. *J. Electroanal. Chem.* **1991**, *315*, 143–160.
(39) Philip, I.; Kaifer, A. E. *J. Org. Chem.* **2005**, *70*, 1558–1564.

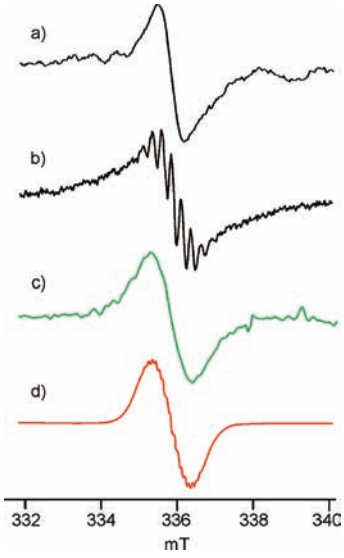

Figure 6. (a) Experimental EPR spectrum of $[^{33}S_4{}^{14}N_4]^{-\bullet}$ at −20 °C after strong digital filtering (black line), (b) experimental EPR spectrum of $[^{33}S_4{}^{14}N_4]^{-\bullet}$ spiked with $[^{32}S_4{}^{14}N_4]^{-\bullet}$ at −20 °C (black line), (c) spectrum of $[^{33}S_4{}^{14}N_4]^{-\bullet}$ after subtraction of the spike and moderate digital filtering (green line), and (d) simulation (red line), with $a(^{33}S_{1-4}) = 0.2$ mT, $a(^{14}N_{1-4}) = 0.12$ mT. g value = 2.0008(1).

apparent variation in LW, while those collected above 0 °C suffer from line-broadening similar to that observed at room temperature.

SEEPR studies of 99% ^{15}N isotope-enriched $^{32}S_4{}^{15}N_4$ were performed in CH_2Cl_2 over the same temperature range. An example of a typical spectrum observed from one 82 s scan at −10 °C is shown in Figure 5c. The characteristic five-line pattern with $a = 0.1635$ mT, LW = 0.05 mT, and intensity ratio 1:4:6:4:1 is consistent with coupling to four equivalent ($I = 1/2$) ^{15}N nuclei. The ratio of $a(^{14}N)/a(^{15}N)$ fits well to the gyromagnetic ratios. In the same way, SEEPR studies were attempted on 99.92% ^{33}S-enriched $^{33}S_4{}^{14}N_4$. The resulting very broad, low-intensity signal (Figure 6a) was difficult to detect, and the sample was subsequently spiked with some natural abundance material. The experimental spectra resulting from reductive electrolysis on samples containing this mixture were easier to detect, facilitating the collection of data with adequate signal-to-noise ratio (Figure 6b). Subtraction of the $[^{32}S_4{}^{14}N_4]^{-\bullet}$ component from the signal followed by digital filtering afforded a broad, undistorted singlet due solely to $[^{33}S_4{}^{14}N_4]^{-\bullet}$ (Figure 6c). A reasonable simulation of this signal is obtained (Figure 6d) by employing the values for $a(^{14}N_{1-4}) = 0.12$ mT and LW = 0.08 mT determined for the $[^{32}S_4{}^{14}N_4]^{-\bullet}$ component before subtraction, and fitting the line shape by including additional coupling from four equivalent S nuclei with $a(^{33}S_{1-4}) = 0.20$ mT. Simulations using two pairs of inequivalent values for $a(^{33}S)$ gave a poorer fit. The DFT (UB3LYP/aug-cc-pVTZ) calculated hfs constants for the static C_{2v} minimum structure of $[S_4N_4]^{-\bullet}$ from our previous report[14] are $a(^{33}S_{1,2}) = -0.65$ and $a(^{33}S_{3,4}) = 0.97$ mT.[40] Exchange can result in averaging of the hfs constants of the interchanged nuclei as seen, for example, in the cyclopentadienyl radical;[41] magnetic interactions between the ^{14}N and ^{33}S nuclei can also lead to more than simple averaging of the couplings such as occurs in the EPR spectrum of dinitrodurene at elevated temperatures.[42] Support for the notion of a rapid conformational equilibrium in $[S_4N_4]^{-\bullet}$ at −20 °C is provided by considering the average of the calculated ^{33}S hfs constants for the two kinds of sulfur nuclei which, at 0.16 mT, is in very good agreement with the ~0.2 mT obtained from the simulation. Note that in the specific case of $[S_4N_4]^{-\bullet}$, lower levels of ^{33}S doping *do not* lead to more easily interpretable EPR spectra.

EPR Investigations of $[S_3N_3]^{\bullet}$. Our previously reported calculations indicate that $[S_3N_3]^{\bullet}$ should possess a planar ring structure (cf. $[S_3N_3]^{-}$), which is mildly distorted toward C_{2v} symmetry as a result of a Jahn−Teller effect.[14] This distortion is reflected in the calculated hfs constants, with two different ^{14}N ($a(N)_{1,2} = 0.57$ mT, $a(N)_3 = -0.18$ mT) and ^{33}S ($a(S)_{1,2} = 0.60$ mT, $a(S)_3 = 0.11$ mT) values. The predicted EPR spectrum based on the calculated isotropic hfs constants with natural abundances of the isotopes is shown in Supporting Information, Figure S3a, along with the high-symmetry spectrum that might result from dynamic exchange with (weighted) average hfs constants ($a(N)_{1-3} = 0.32$ mT, Supporting Information, Figure S3b). There is every reason to have confidence in hfs constants calculated at this level of theory for planar S,N ring compounds.[14]

Our attempts to observe this radical in condensed phases began with low temperature SEEPR studies of CH_2Cl_2 solutions containing either $[Cp_2Co][S_3N_3]$ or $[PPN][S_3N_3]$. Oxidative electrolysis at a potential of −0.2 V at temperatures between −60 and +20 °C did not generate a spectrum that could be conclusively attributed to $[S_3N_3]^{\bullet}$. A persistent five-line pattern was observed (Figure 7), which did not increase in intensity with electrolysis at −0.2 V or decay after stopping electrolysis. The signal did seem to be induced by the presence of the electrodes in solution, and to grow in intensity at lower temperatures. The spectra displayed significant line width variation over the 120 °C temperature range and have a g value of 2.0105. While they could be simulated by using two equivalent nitrogen hfs constants of 0.509 mT, and one (unresolved) nitrogen hfs constant of 0.044 mT, these values do not agree with the calculated hfs as discussed above. Furthermore, the persistent nature of this EPR signal is inconsistent with the estimated lifetime of $[S_3N_3]^{\bullet}$ (vide infra). We did confirm, however, that $[S_3N_3]^{-}$ is oxidized to S_4N_4 during these experiments by generation of the nine-line spectrum of $[S_4N_4]^{-\bullet}$ upon subsequent switching to electrolysis at −1.1 V (Figure 7).

The persistence of the five-line pattern during electrolysis at such negative potentials is also inconsistent with the postulate that it is due to $[S_3N_3]^{\bullet}$. Similar five-line spectra have been seen previously and were assigned to the presence of $[NSN]^{-\bullet}$, a common decomposition product of many unstable S,N species.[3a,43] This species is

(40) The calculated ^{33}S hfs constants for S_4N_4 are $a(^{33}S_{1,2}) = -0.65$ and $a(^{33}S_{3,4}) = 0.97$ mT, i.e., one negative and one positive value; the original report (ref 14.) unfortunately missed the positive sign for $a(^{33}S_{3,4})$.

(41) Liebling, G. R.; McConnell, H. M. *J. Chem. Phys.* **1965**, *42*, 3931–3934.

(42) (a) Freed, J. H.; Fraenkel, G. K. *J. Chem. Phys.* **1962**, *37*, 1156–1157. (b) Sullivan, P. D.; Bolton, J. R. *Adv. Magn. Reson.* **1970**, *4*, 39.

(43) (a) Appel, R.; Ruppert, I.; Milker, R.; Bastian, V. *Chem. Ber.* **1974**, *107*, 380–390. (b) Fritz, H. P.; Bruchhaus, R. *Electrochim. Acta* **1984**, *29*, 947–950. (c) Domschke, G.; Mayer, R.; Bleisch, S.; Bartl, A.; Stako, A. *Magn. Reson. Chem.* **1990**, *28*, 797–806.

Table 4. Experimental and Calculated EPR Data for $[S4N4]^{-\bullet}$

nucleus	expt hfs (mT)	calc hfs (mT)[14]	line width (mT)	*g* value	solvent
$^{14}N_{1-4}$ [a]	0.1185(1)[3b]	0.08	0.046	2.0006(1)	THF
$^{14}N_{1-4}$ [b]	0.117(2)[3c]	0.08	0.05	not reported	CH_3CN
$^{14}N_{1-4}$ [c]	0.1175	0.08	0.06	2.0008(1)	CH_2Cl_2
$^{15}N_{1-4}$ [c]	0.1635		0.05	2.0008(1)	CH_2Cl_2
$^{33}S_{1,2}$ [d]	0.2	−0.65[40]	0.08	2.0008(1)	CH_2Cl_2
$^{33}S_{3,4}$ [d]	0.2	0.97[40]	0.08	2.0008(1)	CH_2Cl_2

[a] $[^nBu_4N][ClO_4]$ as the supporting electrolyte, −25 °C. [b] $[Et_4N][ClO_4]$ as the supporting electrolyte, −20 °C. [c] 1.2 mM solution with 0.4 M $[^nBu_4N][PF_6]$ as the supporting electrolyte, −10 °C. [d] 5.4 mM solution with 0.4 M $[^nBu_4N][PF_6]$ as the supporting electrolyte, −20 °C.

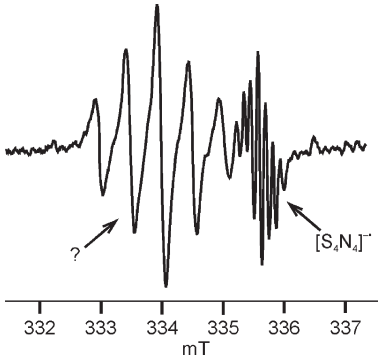

Figure 7. Experimental first derivative EPR spectra obtained during in situ reductive electrolysis of $[PPN][S_3N_3]$ at −1.1 V (82 s single scan) following initial electrolysis at −0.2 V at a gold mesh electrode at −60 °C in CH_2Cl_2 (0.4 M $[^nBu_4N][PF_6]$), modulation amplitude = 0.2 mT. *g* values = 2.0105 (left signal), 2.0008 (right signal).

reported to possess equivalent ^{14}N nuclei with $a(N)$ ~0.50−0.52 mT and to have *g* values in the range 2.0105(5) to 2.0103, which fits well with the signal we observe. The line width dependence that we observed for this signal, apparently for the first time, would also seem to be more consistent with a bent σ radical than with a planar π-radical. We do not know how the species causing this signal arises, but the following observations can be made: (i) this EPR signal is never seen during electrolysis of pure S_4N_4 solutions; (ii) it does not increase in intensity in response to electrolysis over the potential range 0 to −1.3 V. Though $[NSN]^{-\bullet}$ could arise from disproportionation of $[S_3N_3]^{\bullet}$ (along with the known $[SNS]^+$ ion),[14] this cannot be the dominant decomposition pathway in view of observation (ii).

As an alternative route to $[S_3N_3]^{\bullet}$, we carried out bulk reductive electrolysis of S_4N_4 in CH_2Cl_2 at −1.25 V, followed by transfer of the newly generated $[^nBu_4N][S_3N_3]$ solution to the SEEPR cell, and then performing in situ oxidative electrolysis of $[S_3N_3]^-$. This led to results very similar to those found when using $[Cp_2Co][S_3N_3]$ and $[PPN][S_3N_3]$ for such experiments. The bulk oxidative electrolysis of a CH_2Cl_2 solution containing $[Cp_2Co][S_3N_3]$ at −0.2 V was also attempted. Aliquots of the oxidized solution were syringed out at 1 min intervals into EPR tubes and frozen in LN_2 and inserted into the EPR cavity. No notable EPR signals were detected from any of the frozen aliquots collected. All attempts to detect $[S_3N_3]^{\bullet}$ have thus far been unsuccessful, corroborating earlier failures reported by other workers.[10,16]

EPR Lifetime Measurements. Rate constants from the decay of the EPR signal of $[S_4N_4]^{-\bullet}$ in CH_2Cl_2 at temperatures between −88.4 and +25.6 °C and concentrations of 2 and 5 mM were determined by generating the radical electrochemically, halting electrolysis, and measuring the decay of the signal intensity as a function of time at constant field. The slope of the plots of $\ln(C_t/C_{t=0})$ versus *t* (*C* = signal intensity) yielded k_{f1} values in the range of 0.0052−1.85 s^{-1} over a 70 °C temperature range (Supporting Information, Table S4). Plots that were based on second-order kinetics exhibited a much poorer fit to the data, consistent with a previous report.[3c] The accuracy of k_{f1} values was found to be negatively affected at lower temperatures by a competing factor, the diffusion of the radical anion out of the EPR cavity more rapidly than its actual decay (see Supporting Information, Figures S4, S5). Therefore only rate constants between the temperatures of −22 and +16 °C were used in an Arrhenius activation energy plot (Supporting Information, Figure S6); which yielded a value of 62 ± 2 kJ/mol. This value is slightly higher than the literature value of 47±4 kJ/mol,[3c] which may be due to the different solvent used in our study, but also may suggest that the statistical uncertainty in such measurements significantly underestimates the true errors.

Simulations of the Cyclic Voltammetric Responses for S_4N_4 and $[S_3N_3]^-$. Full digital simulations of the CV responses were carried out to obtain kinetic data for the $[S_4N_4]^{-/0}$ and $[S_3N_3]^{-/0}$ redox couples in solutions of S_4N_4, $[Cp_2Co][S_3N_3]$, and $[PPN][S_3N_3]$. All simulations employed independently measured values for the electrode area, analyte concentration, temperature, diffusion coefficient *D*, and uncompensated solution resistance R_u. Values for *D* (Table 1) for both S_4N_4 and $[S_3N_3]^-$ were obtained from RDE voltammetry experiments, and were assumed to be equivalent for the corresponding oxidized or reduced counterparts.

$[S_4N_4]^{-/0}$. Digital simulations of CVs obtained for the $[S_4N_4]^{-/0}$ redox couple over a range of scan rates v = 0.1−0.5 V s^{-1} at two concentrations were performed to quantify the decay of the reduction product as described by an EC mechanism:[44]

$$[S_4N_4] + e^- \underset{k_{s-1}}{\overset{k_{s1}}{\rightleftarrows}} [S_4N_4]^{-\bullet} \qquad (E^{0/}_{(1)}, k_{s1}, \alpha) \qquad (3)$$

$$[S_4N_4]^{-\bullet} \underset{k_{b1}}{\overset{k_{f1}}{\rightleftarrows}} [S_3N_3]^- + [NS]^{\bullet} \qquad (K_{eq1}, k_{f1}) \qquad (4)$$

where k_s and α are, respectively, the standard heterogeneous rate constant and the transfer coefficient associated

(44) For the EC and ECC classifications of heterogeneous electron transfer reactions (E) with coupled homogeneous chemical reactions (C), see chapter 12 of ref 21, pp 471−478.

with the Butler−Volmer formalism[21] for a heterogeneous electron transfer; K_{eq1} and k_{f1} are the equilibrium constant and the rate constant for the follow-up chemical reaction. The first-order nature of the decay of $[S_4N_4]^{-\bullet}$ was previously established in the more polar solvent CH_3CN,[3c] and values for k_{f1} at approximately the same temperature obtained in that study were used as a starting point for our own investigations. Several second-order decay mechanisms were also considered, and in all cases these failed to reproduce the experimental CVs over more than one concentration. Many possibilities were also considered for the first-order decay pathway of the radical anion, which is known to lead ultimately to $[S_3N_3]^-$. ECC mechanisms[44] which included an intermediate between $[S_4N_4]^{-\bullet}$ and $[S_3N_3]^-$ had parameters for the second C step that did not affect the overall fit, so ECC was abandoned from consideration for this redox couple.

For the EC mechanism,[44] the adjustable parameters were the apparent $E^{0\prime}{}_{(1)}$ as measured versus the silver-wire quasi reference electrode (see Table 3 for $E^{0\prime}$ values versus $E_{Fc^{0/+}}{}^{0\prime}$), k_{f1}, and k_{s1}. For the purposes of simulation the value of α was assumed to be 0.5. Various values for the equilibrium constant K_{eq1} were investigated, but small values did not lead to optimal fits, so this value was arbitrarily fixed at 10^6, thus rendering the chemical reaction effectively irreversible over the scan rates investigated. The optimization of simulated CV responses using DigiElch was deemed successful when the simulated and experimental peak heights and positions overlaid each other (see Supporting Information, Figure S7). Values for the rate constants were determined from fitting CVs obtained at two different concentrations measured over the scan rate range $v = 0.1-0.5$ V s^{-1} (see Supporting Information, Table S3) and led to estimates of these values as $k_{s1} = 0.034 \pm 0.004$ cm s^{-1} and $k_{f1} = 1.8 \pm 0.2$ s^{-1}. Thus, full line-shape digital simulation of the CVs are consistent with a slow rate of electron transfer to S_4N_4 (i.e., charge-transfer irreversibility, confirming the observations of Williford et al. from their study in $CH_3CN/[Et_4N][ClO_4]$ below 0 °C),[3c] followed by first-order decay of the initially formed $[S_4N_4]^{-\bullet}$.

$[S_3N_3]^{-/0}$. Digital simulations of CVs obtained for the $[S_3N_3]^{-/0}$ redox couple using both $[Cp_2Co][S_3N_3]$ and $[PPN][S_3N_3]$ as sources of the anion were undertaken using a similar regime to that employed in the previous section, and focused on quantifying the decay of the oxidation product as described by the EC mechanism:[44]

$$[S_3N_3]^{\bullet} + e^- \underset{k_{s-2}}{\overset{k_{s2}}{\rightleftarrows}} [S_3N_3]^- \qquad (E^{0\prime}_{(2)}, k_{s2}, \alpha) \qquad (5)$$

$$[S_3N_3]^{\bullet} \underset{k_{b2}}{\overset{k_{f2}}{\rightleftarrows}} S_4N_4 \qquad (K_{eq2}, k_{f2}) \qquad (6)$$

where k_s, α, K_{eq}, and k_f have the same meanings as described previously. Exclusion of any coupled homogeneous chemical steps subsequent to the initial electron transfer failed to accurately reproduce the CVs, consistent with previous evidence for the conversion of $[S_3N_3]^-$ to S_4N_4 following oxidative electrolysis.[10] Anomalous deviations in the peak current heights led to complications in simulating the CVs, and could be traced to a hypersensitivity of the anion toward oxygen (see Supporting Information for details on how this was overcome). CVs obtained under a rigorous exclusion of oxygen were simulated to determine values for the electron transfer k_{s2} and the decay step k_{f2} rate constants. Both first- and second-order decay mechanisms were considered. Those which considered the radical to react with itself (dimerization) or with $[S_3N_3]^-$ failed to reproduce the CVs. For the EC mechanism described above, the adjustable parameters were the apparent $E^{0\prime}{}_{(2)}$ (see Table 4 for $E^{0\prime}$ values versus $E_{Fc^{0/+}}{}^{0\prime}$), k_{f2}, and k_{s2}. The value of α was assumed to be 0.5. Various values for the equilibrium constant K_{eq2} were investigated, but small values for did not lead to optimal fits, and thus this value was again arbitrarily fixed at 10^6. This resulted in good overlap of the simulated and experimental peak heights and positions (Supporting Information, Figures S9, S10). Final values for k_{s2} and k_{f2} were determined from fitting CVs obtained at two different concentrations measured over the scan rate range $v = 0.1-0.5$ V s^{-1} (see Supporting Information, Table S6) giving estimates of these values of $k_{s2} = 0.022 \pm 0.005$ cm s^{-1} and $k_{f2} = 0.4 \pm 0.1$ s^{-1}. Thus there is also a slow rate of electron transfer for the oxidation of $[S_3N_3]^-$, followed by an apparent first-order chemical decomposition of the electrogenerated species, which we presume to be the elusive neutral radical $[S_3N_3]^{\bullet}$.

Scheme 1. Simplified "Square Scheme" Mechanism for the Interconversion of S_4N_4 and $[S_3N_3]^-$ Following First-Order Decay Pathways for Both Chemical Steps[a]

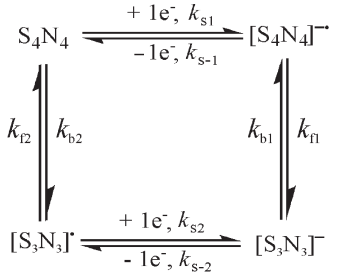

[a] The parameters used here are those defined in eqs 3−6.

$[S_4N_4]^{-/0}$−$[S_3N_3]^{-/0}$ Interconversion with First-Order Decay. Building on the successful simulations of the individual redox couples we set out to characterize the interconversion of the two electroactive species. While the interconversion is necessarily complex because of the 4:3 stoichiometry (as confirmed by bulk electrolysis), our attempts to incorporate this into the kinetic model were not successful. In the end we applied a simplified "square scheme" mechanism,[45] depicted in Scheme 1, which simply combines the parameters developed above for the two redox couples independently. We start by simulating CVs obtained on solutions containing bulk S_4N_4 over a larger potential window (−0.2 to −1.15 V, Figure 8).

(45) (a) Evans, D. H. *Chem. Rev.* **1990**, *90*, 739–751. (b) Lerke, S. A.; Evans, D. H.; Feldberg, S. W. *J. Electroanal. Chem.* **1990**, *296*, 299–315. (c) Balducci, G.; Costa, G. *J. Electroanal. Chem.* **1993**, *348*, 355–365. (d) González-Fernández, C. F.; García-Hernández, M. T.; Horno, J. *J. Electroanal. Chem.* **1995**, *395*, 39–44. (e) González-Fernández, M. T.; Castilla, J.; García-Hernández, C. F.; Horno, J. *J. Electroanal. Chem.* **1997**, *424*, 207–212. Note that in conventional settings of the square scheme, the reaction proceeds from top left to bottom right along both branches. The definitions used in Schemes 1 and 2 are designed for consistency with our prior treatments of the two components separately. Harmonization with the treatments in the cited references is readily accomplished by inverting the k_f and k_b terms for the left branch of the scheme.

In the full-cycle simulations, the adjustable parameters were $E^o_{(1)}$, $E^o_{(2)}$, k_{f1}, and k_{f2}. The value of α was again assumed to be 0.5. Including k_{s1} and k_{s2} as adjustable parameters resulted in only minor variations in their values (within standard deviation error limits), and therefore these were kept fixed to the average values determined previously ($k_{s1} = 0.03$ cm s^{-1}, $k_{s2} = 0.02$ cm s^{-1}) to limit the number of adjustable parameters. $K_{eq\ 1}$ was also kept fixed at 10^6 as before, but in the square scheme this makes K_{eq2} a dependent variable and these parameters are reported among the final fits for completeness (see Table 5).[45]

Values for k_{f1} and k_{f2} leading to the best possible overlap of the simulated and experimental peak heights and positions are listed in Table 5; k_{f2} values are in excellent agreement with those determined in the $[S_3N_3]^{-/0}$ study, and k_{f1} values are just outside the standard deviation determined from the $[S_4N_4]^{-/0}$ study. Choosing to fix the parameters k_{f1} and k_{f2} to the average values calculated from the previous studies (k_{f1} = 1.8 s^{-1}, k_{f2} = 0.4 s^{-1}) showed only minor deviations in the overlap of the simulated versus the experimental peak heights. It is probable that the statistical uncertainty for the k_{f1} values obtained in the $[S_4N_4]^{-/0}$ study underestimates the true errors.

To ensure the general validity of these parameters, simulations of CV measurements covering a similar extended potential range (−0.15 to −1.1 V) starting from solutions of [PPN][S_3N_3] were also undertaken (Figure 9). The adjustable parameters were again $E^o_{(1)}$, $E^o_{(2)}$, k_{f1}, and k_{f2}. k_{s1} and k_{s2} were again kept fixed at 0.03 and 0.02, respectively, and K_{eq1} was fixed at 10^6. Once again the k_{f2} values are in excellent agreement with those determined previously, but values for k_{f1} are just outside of the standard deviation from the $[S_4N_4]^{-/0}$ study. These results are also compiled in Table 5 and from a conservative comparison of the four data sets from two chemically different species, *best estimates* for the key parameters have been determined as follows: $k_{s1} = 0.034 \pm 0.004$ cm s^{-1}, $k_{f1} = 2.0 \pm 0.5$ s^{-1}, $k_{s2} = 0.022 \pm 0.005$ cm s^{-1}, and $k_{f2} = 0.4 \pm 0.2$ s^{-1}. We note that these values using the higher estimated errors are all, within experimental error, the same as those determined for the individual redox couples. Moreover, k_{f1} is in qualitative agreement with rates determined from EPR lifetimes (Supporting Information, Table S4). The success of this simple square scheme would then seem to indicate that other processes occurring in solution, such as the elimination of the [NS]$^\bullet$ radical from $[S_4N_4]^{-\bullet}$ or the recombination of the former to reform S_4N_4 are not rate-determining.

$[S_4N_4]^{-/0}$ $[S_3N_3]^{-/0}$ Interconversion with Involvement of [NS]$^\bullet$. With a calculated k_{f2} value of 0.4 s^{-1} for the decay of the oxidation product of $[S_3N_3]^-$ ($t_{1/2}$ = 1.7 s at RT), we became even more surprised by our inability to obtain an EPR spectrum of $[S_3N_3]^\bullet$, including measurements taken down to −60 °C, especially given the excellent EPR results for $[S_4N_4,]^{-\bullet}$ with its almost 5 times larger k_{f1} value ($t_{1/2}$ = 0.69 s) at RT. So we returned to the simulations of the CV measurements to consider another alternative for the decay of the oxidation product of $[S_3N_3]^-$. The alternate pathway that was considered was suggested by careful inspection of concentration profiles generated in DigiElch in the simulations starting from bulk S_4N_4 over an extended potential window to include both redox couples (Figure 10). This profile indicates that an approximately 23% [NS]$^\bullet$ concentration is generated at the electrode surface throughout a CV cycle. We postulated that if this quantity of [NS]$^\bullet$ could exist in a solution of

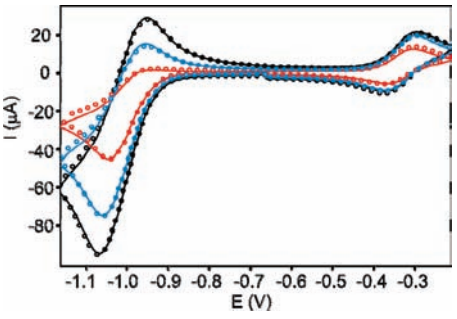

Figure 8. Comparison of the experimental CVs of 2.40 mM S_4N_4 over an extended potential window at 0.1 (red line), 0.3 (blue line), and 0.5 (black line)V·s^{-1} (GC electrode), 0.4 M [^{n}Bu$_4$N][PF_6] in CH_2Cl_2 at 21.1 °C, along with the simulated CVs (0.1 V s^{-1} = red circles, 0.3 V s^{-1} = blue circles, 0.5 V s^{-1} = black circles). See Table 5 for simulation parameters.

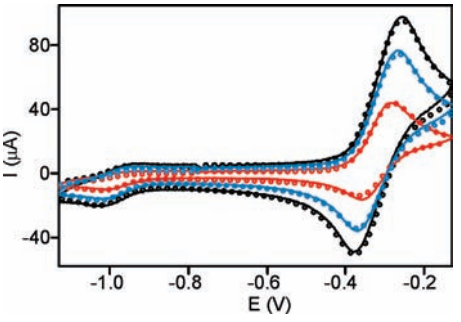

Figure 9. Comparison of the experimental CVs of 3.90 mM [PPN][S_3N_3] over an extended potential window at 0.1 (red line), 0.3 (blue line), and 0.5 (black line)V·s^{-1} (GC electrode), 0.4 M [^{n}Bu$_4$N][PF_6] in CH_2Cl_2 at 21.5 °C, along with the simulated CVs (0.1 V s^{-1} = red circles, 0.3 V s^{-1} = blue circles, 0.5 V s^{-1} = black circles). See Table 5 for simulation parameters.

Table 5. Parameters Used in Full Cycle CV Simulations Based on Scheme 1 in CH_2Cl_2 on a GC Electrode[a]

bulk cmpd	conc (mM)[b]	R_u, Ω[c]	$\|\Delta E^{o\prime}\|$ (V)[d]	k_{f1} (s^{-1})	K_{eq1} (×10^6)[e]	k_{f2} (s^{-1})	K_{eq2} (×10^5)[e]	T (°C)
S_4N_4	2.40	244	0.67	1.54 ± 0.07	1.00	0.40 ± 0.18	2.5 ± 0.3	21.1
S_4N_4	1.20	222.5	0.66	1.65 ± 0.08	1.00	0.50 ± 0.25	2.0 ± 0.2	23.3
[PPN][S_3N_3]	3.90	242.2	0.65	2.62 ± 1.30	1.00	0.39 ± 0.14	1.5 ± 0.1	21.5
[PPN][S_3N_3]	8.20	238.2	0.65	2.77 ± 0.67	1.00	0.46 ± 0.11	1.7 ± 0.5	19.3
Best est.			0.66	2.0 ± 0.5	1.00	0.4 ± 0.2	1.9 ± 0.5	21 ± 2

[a] Invariant parameters: D (S_4N_4, $[S_4N_4]^{-\bullet}$) = 1.17 × 10^{-5} cm^2 s^{-1}, D ($[S_3N_3]^-$, $[S_3N_3]^\bullet$) = 4.00 × 10^{-6} cm^2 s^{-1}, as determined by RDE measurements (see Table 1). v = 0.1−0.5 V s^{-1}. k_{s1} = 0.03 cm s^{-1} k_{s2} = 0.02 cm s^{-1} as determined from the average of the values listed in Supporting Information, Tables S5, S6. [b] Invariant parameters determined by original solution composition. [c] R_u values were measured on a PARSTAT 2273 potentiostat. [d] For the experimental potentials vs Fc see Table 3. [e] K_{eq1} was fixed at a high value after considerable testing of alternatives; K_{eq2} is a dependent variable.

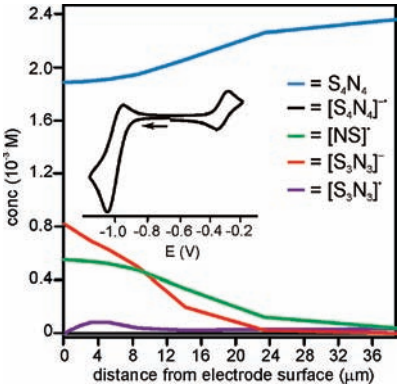

Figure 10. Concentration profile generated from a 2.40 mM S_4N_4 solution and using parameters generated from Scheme 2. The quantity of each species is given subsequent to one complete CV cycle, starting from and ending at −0.7 V, at and beyond the surface of the electrode.

Scheme 2. Alternative "Square Scheme" Mechanism for the Involvement of $[NS]^{\bullet}$ in the Interconversion of S_4N_4 and $[S_3N_3]^-$[a]

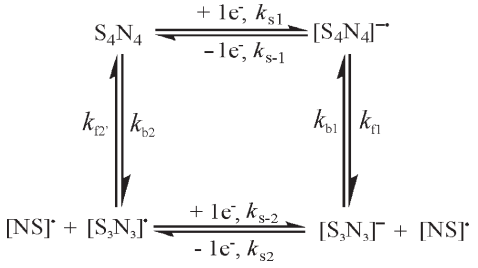

[a] The second chemical step is now second-order with Rate = $k_{f2'}[S_3N_3][NS]$.

S_4N_4, then it was plausible for similar amounts to exist in a solution of $[S_3N_3]^-$. Therefore, we assumed an approximately 20% $[NS]^{\bullet}$ equilibrium concentration in solutions of $[PPN][S_3N_3]$ in the presence of a poised electrode surface which could then react with $[S_3N_3]^{\bullet}$ to regenerate S_4N_4. This results in a second-order pathway for this step, as described by Scheme 2. However, the $[NS]^{\bullet}$ radical is expected to be EPR-silent in condensed phases[3h] and it was not observed in our EPR investigations.

The same experimental data were then fitted to the new mechanism. The adjustable parameters for this study were $E^o_{(1)}$, $E^o_{(2)}$, k_{f1}, and $k_{f2'}$. Again, k_{s1} and k_{s2} were kept fixed at 0.03 and 0.02, respectively, and again K_{eq1} was fixed at 10^6, with K_{eq2} as the dependent variable. The fits obtained are comparable to those attained using Scheme 1 and the results are listed in Table 6. However, the fits starting from bulk solutions of $[PPN][S_3N_3]$, unlike S_4N_4, required the inclusion of an $[NS]^{\bullet}$ bulk concentration term. These fits resulted in a best estimate for the second-order rate constant k_{f2} sub prime (spm) of $1.1 \pm 0.3 \times 10^3$ s^{-1} M^{-1} and unchanged values for the other parameters. In this case the rate is proportional to the product of two different concentrations for the second-order reaction (see Supporting Information). Solving for $t_{1/2}$ results in lifetimes for $[S_3N_3]^{\bullet}$ in the range of 0.2 to 0.8 s, which are shorter than that estimated from the first-order decay pathway. This may be significant in terms of our inability to detect an EPR signal for this radical. One of the reviewers suggested that dimerization of the radical might still be a factor despite our inability to detect such a process in the voltammetric modeling. A dimer structure has been detected by gas-phase DFT calculations as shown in Supporting Information, Figure S11 but the interaction does not appear to be strong. Related sulfur−nitrogen heterocyclic radicals in dilute, cold, solutions are well-known to give EPR signals that are easy to detect even though in the solid-state they form dimers. It is certainly the case, however, that dimerization may explain the null results obtained from the frozen solution spectra. Ultimately we still do not have a good explanation for the apparent EPR silence of this free radical.

Chemical Mechanisms for the Interconversion of S_4N_4 and $[S_3N_3]^-$. The possible mechanisms for the interconversion of S_4N_4 and $[S_3N_3]^-$ are discussed in the light of the detailed kinetic data provided by the digital simulations of the CVs. We start by considering the decomposition of $[S_4N_4]^{-\bullet}$, which obeys first-order kinetics and is not influenced by the concentration of S_4N_4. The previously reported[3c] activation energy for this decomposition of 47 ± 4 kJ mol^{-1}, along with our new value in CH_2Cl_2 of 62 ± 2 kJ mol^{-1} is consistent with a vibrationally induced 1,3 nitrogen shift mechanism (Scheme 3) similar to what has been invoked to explain ring contractions for a variety of S,N heterocycles, that is, dithiatetrazocine radical anions (**3**)[12] and trithiatetrazocines (E_A = 67 ± 4 kJ mol^{-1}),[46a] as well as the exchange processes that occur in bicyclic CN_5S_3 ($E_A = 84 \pm 4$ kJ mol^{-1})[46b−46d] and $[S_4N_5]^+$ cages.[47] The recent investigation of the photochemical activation of S_4N_4 in argon matrixes identified three intermediates, including a six-membered S_3N_3 ring carrying an exocyclic −N═S group analogous to the proposed intermediate [*cyclo*-S_3N_3−N═S]$^{-\bullet}$ (PBE1PBE/(aug)cc-pVTZ calculated structure, Supporting Information, Figure S12) shown in Scheme 3 (bottom right).[11,48]

With respect to the (re)oxidation of $[S_3N_3]^-$, it is evident that the purported $[S_3N_3]^{\bullet}$ radical reverts rapidly to S_4N_4. The kinetics demonstrate that decomposition may follow either a first-order or second-order pathway. For the first-order case, elimination of $[NS]^{\bullet}$ from $[S_3N_3]^{\bullet}$ would produce S_2N_2.[1] It has been predicted that S_2N_2 in the presence of nucleophiles or reducing agents will rapidly form S_4N_4.[2] Direct recombination of $[NS]^{\bullet}$ with $[S_3N_3]^{\bullet}$ is equally plausible given the evidence from the voltammetry study for a second-order recombination path along with the value of K_{eq1} which indicates that the concentration of $[NS]^{\bullet}$ is appreciable. We note that the intermediates *cyclo*-S_3N_3−N═S and *cyclo*-S_3N_3−S≡N identified by Zibarev et al. upon photochemical excitation may afford a direct

(46) (a) Boeré, R. T.; Cordes, A. W.; Oakley, R. T. *J. Am. Chem. Soc.* **1987**, *109*, 7781–7785. (b) Bestari, K. T.; Boeré, R. T.; Oakley, R. T. *J. Am. Chem. Soc.* **1989**, *111*, 1579–1584. (c) Boeré, R. T.; Oakley, R. T.; Shevalier, M. *J. Chem. Soc., Chem. Commun.* **1987**, 110–112. (d) Boeré, R. T.; Cordes, A. W.; Craig, S. L.; Graham, J. B.; Oakley, R. T.; Privett, J. A. J. *J. Chem. Soc., Chem. Commun.* **1986**, 807–808.

(47) Bartetzko, R.; Gleiter, R. *Chem. Ber.* **1980**, *113*, 1138–1144.

(48) The excited-state isomer of neutral tetrasulfur tetranitride [*cyclo*-S_3N_3—N═S] is a stable calculated gas-phase species by DFT methods (see ref 11). In our own work we have calculated the corresponding radical anion [*cyclo*-S_3N_3—N═S]$^{-\bullet}$ at the PBE1PBE/(aug)cc-pVTZ level of theory, the structure of which is somewhat less symmetrical than that of the neutral analog (Figure S12). However, we have not yet succeeded in tracing the path of the 1,3-N shift reaction shown in Scheme 3 computationally and therefore refrain from further discussion at this time. That such similar structure postulates are made for intermediates in photochemical (ref 11) and electrochemical (this work) activation of the cage structure of S_4N_4 is, we believe, of significance.

Table 6. Parameters Used in Full Cycle CV Simulations Based on Scheme 2 in CH_2Cl_2 on a GC Electrode[a]

bulk cmpd[b]	conc $[NS]^{\bullet}$ (mM)[c]	$\lvert\Delta E^{o\prime}\rvert$ (V)[d]	k_{f1} (s^{-1})	K_{eq1} ($\times 10^6$)[e]	$k_{f2'}$ ($\times 10^3$ s^{-1} M^{-1})	K_{eq2} ($\times 10^5$)[e]	T (°C)
S_4N_4	0	0.67	1.53 ± 0.06	1.00	0.70 ± 0.40	2.6 ± 0.3	21.1
S_4N_4	0	0.67	1.61 ± 0.05	1.00	1.36 ± 0.35	2.2 ± 0.2	23.3
[PPN][S_3N_3]	0.80	0.65	2.79 ± 1.36	1.00	1.25 ± 0.15	1.6 ± 0.1	21.5
[PPN][S_3N_3]	1.60	0.65	2.95 ± 0.67	1.00	1.19 ± 0.49	1.7 ± 0.5	19.3
best est.		0.66	2.2 ± 0.5	1.00	1.1 ± 0.3	2.0 ± 0.3	21 ± 2

[a] Invariant parameters: D (S_4N_4, $[S_4N_4]^{-\bullet}$) $= 1.17 \times 10^{-5}$ cm^2 s^{-1}, D ($[S_3N_3]^-$, $[S_3N_3]^{\bullet}$) $= 4.00 \times 10^{-6}$ cm^2 s^{-1}, as determined by RDE measurements (see Table 1). $v = 0.1-0.5$ V s^{-1}. $k_{s1} = 0.03$ cm s^{-1} $k_{s2} = 0.02$ cm s^{-1} as determined from the average of the values listed in Supporting Information, Tables S5, S6. [b] For the concentration of the bulk compound and R_u values, see Table 5. [c] As determined from the simulations only. [d] For the experimental potentials vs Fc, see Table 3. [e] K_{eq1} was fixed at a high value after considerable testing of alternatives; K_{eq2} is a dependent variable.

Scheme 3. Formation of $[S_3N_3]^-$ and $[NS]^{\bullet}$ from $[S_4N_4]^{-\bullet}$ by a Sigmatropic 1,3 Nitrogen Shift Mechanism

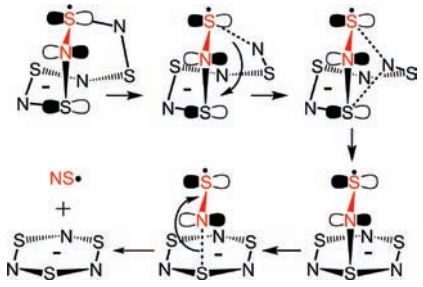

pathway for the recombination of $[NS]^{\bullet}$ with $[S_3N_3]^{\bullet}$ via concerted reactions between their respective π systems.[11] Dimerization of $[NS]^{\bullet}$ is expected to lead to S_2N_2, although Mawhinney and Goddard determined that in the gas phase the only such product is the linear NS−SN.[49] Thus several paths might well operate simultaneously for the conversion of $[S_3N_3]^{\bullet}$ to S_4N_4.

Electronic Structure of $[S_3N_3]^{\bullet}$. The electronic structure of $[S_3N_3]^{\bullet}$ has most recently been examined by us using density functional theory (DFT).[14] The calculations fully supported a planar ring geometry with a $^2A_2$ ground state, in excellent agreement with the previous Hartree−Fock and CI calculations employing basis sets of minimal and double-ζ quality.[15] The radical has C_{2v} symmetry but the geometrical distortions are very small when the optimized structure is contrasted with that of the diamagnetic D_{3h} symmetric $[S_3N_3]^-$ anion.[4] The symmetry lowering upon detachment of an electron is readily understood by noting that the highest occupied molecular orbitals of $[S_3N_3]^-$ form an e″ symmetric degenerate pair. Thus, the radical undergoes a first-order Jahn−Teller distortion to displace the nuclei to new equilibrium positions of lower symmetry, causing a splitting of the e″ level to two orbitals which transform as b_1 and a_2 in the C_{2v} point group.

The ground state electronic configuration of $[S_3N_3]^{\bullet}$ is $...(5b_1)^2(3a_2)^1(6b_1)^0...$ based on the occupation of the orbitals in the Kohn−Sham reference determinant.[14] However, the energy separation of the highest doubly and singly occupied orbitals is found to be only 0.01 hartree. This is not entirely unexpected considering that the $5b_1$ and $3a_2$ orbitals originate from the initially degenerate pair and that the molecular framework is very close to being of higher D_{3h} symmetry. It is therefore probable that the lowest $^2B_1$ state with a configuration $...(3a_2)^2(5b_1)^1(6b_1)^0...$ is energetically similar to the $^2A_2$ state and that the DFT calculation converged to one of the two possibilities by coincidence. Since DFT is in general not the method of choice to examine the properties of wave functions, we decided to conduct a thorough analysis of the ground state of $[S_3N_3]^{\bullet}$ using a variety of ab initio methods.

The first signs of the peculiarities in the ground state wave function of $[S_3N_3]^{\bullet}$ are observed in HF single point calculations which, even when started from the DFT optimized geometry, do not converge after 120 iterations (Gaussian) or converge to a highly improbable $^2A_1$ state (Molpro). Enforcing the symmetry of the wave function to be A_2 helps in both cases after which the HF calculations converge to the same solution as found using DFT. However, an analysis of the HF SCF iterations shows that the convergence problem is not initiated by two close-lying electronic states of different symmetry but rather two close-lying configurations belonging to the same A_2 representation of the C_{2v} point group. Hence, we conclude that the ground state wave function of $[S_3N_3]^{\bullet}$ appears to be multideterminantal in character. This was confirmed by conducting CAS calculations; MP2 and CCSD calculations were also performed for comparative purposes.

The [3,3]-CAS optimizations unequivocally established that the ground state of $[S_3N_3]^{\bullet}$ has $^2A_2$ symmetry; the optimized structure is also in good agreement with the DFT results. The CI vector coefficients indicate that the ground state wave function is a linear combination of five Slater determinants which form two configurations: the "closed shell doublet" configuration $(5b_1)^2(3a_2)^1(6b_1)^0-(5b_1)^0(3a_2)^1(6b_1)^2$ and the "doublet triradical" configuration $(5b_1)^1(3a_2)^1(6b_1)^1$. The latter configuration is a linear combination of three Slater determinants differing only with respect to the spin state of the electrons (1/2,−1/2,1/2; 1/2,1/2,−1/2 and −1/2,1/2,1/2) thereby ensuring that the wave function is a true eigenstate of both S_z and S^2 operators. The most important configurations in the ground state wave function of $[S_3N_3]^{\bullet}$ are depicted in Figure 11 along with the pictures of frontier orbitals.

The wave function analysis shows that the doublet $^2A_2$ state of $[S_3N_3]^{\bullet}$ is considerably more complex than what can be inferred from the DFT result alone: the near degeneracy of the $5b_1$, $3a_2$, and $6b_1$ orbitals allows three electrons to be distributed in three orbitals giving rise to a small triradical component in the wave function. The triradical character in $[S_3N_3]^{\bullet}$ is sufficiently small to allow its treatment with modern exchange-correlation functionals and, hence, its presence remains unnoticed within the density functional formalism of electronic structure theory. Triradicals with an open-shell doublet ground state have been of increasing experimental and theoretical

(49) Mawhinney, R. C.; Goddard, J. D. *Inorg. Chem.* **2003**, *42*, 6323–6337.

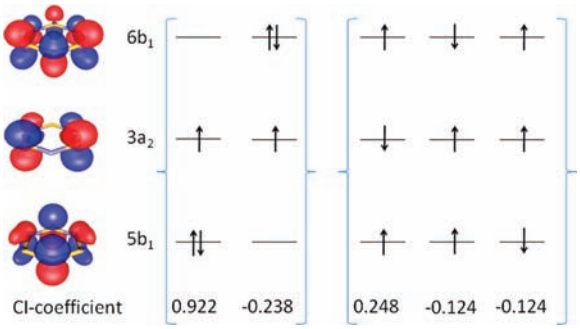

Figure 11. Frontier MOs (isosurface value ± 0.05) and leading configurations in the wave function of $[S_3N_3]^{\bullet}$.

interest during recent years[50] and $[S_3N_3]^{\bullet}$ represents an interesting addition to the growing continuum of such systems. Since the ground state wave function of $[S_3N_3]^{\bullet}$ is dominated by the closed-shell doublet configuration, it is not a true triradical species but can be best viewed as a *triradicaloid*. This is also evident from the calculated (adiabatic) doublet-quartet splitting which is as large as -120 kJ mol^{-1}. The electronic structure of $[S_3N_3]^{\bullet}$ can therefore be contrasted to that of S_2N_2 in which the energetic proximity of the highest occupied (HOMO) and the lowest unoccupied molecular orbital (LUMO) induces a small, but nevertheless significant, singlet diradical character to the wave function.[51]

As in the case of S_2N_2,[51] the failure in Hartree−Fock to describe the electronic structure of $[S_3N_3]^{\bullet}$ is best seen when calculating molecular properties. For example, the vibrational frequencies of $[S_3N_3]^{\bullet}$ show differences up to 300 cm^{-1} when the HF and DFT values are compared. It is interesting to note that MP2 suffices much better and predicts harmonic vibrational frequencies in reasonable qualitative and quantitative agreement with CCSD and DFT. However, the above does not hold for the band intensities since the most intense IR-transition at the MP2 level of theory, the lowest b_2 symmetric normal mode, has practically no intensity when the calculations are done using either density functional or coupled cluster methods. The failure of MP2 in describing $[S_3N_3]^{\bullet}$ is also apparent from the calculated natural orbital occupation numbers (NOONs), which show one value significantly higher than two (2.13) and one much lower than zero (−0.16). The presence of negative NOONs in the MP2 wave function has been found to be highly indicative of the need for a multiconfigurational description of the system.[52] In addition, the [3,3]-CAS NOON for the $6b_1$ orbital is 0.21 but the MP2 value is significantly lower, 0.04, giving a clear sign of the poor description of the frontier orbitals within the latter method. However, the CAS calculation used a minimum active space which is significantly smaller than the full valence space generally required to obtain essentially converged orbital occupancies. Hence, in view of the minor triradical character in $[S_3N_3]^{\bullet}$, the orbital occupation numbers calculated from the CCSD wave function should be considered the most accurate. Rather expectedly, all NOONs are found to be between 0 and 2 at the CCSD level, and the calculated occupations for the $5b_1$, $3a_2$, and $6b_1$ frontier orbitals are 1.88, 0.96, and 0.13, respectively, in good qualitative agreement with the CAS CI-vector coefficients. However, it is not obvious what effect triradicaloid character in the ground state wave function of $[S_3N_3]^{\bullet}$ might have on the EPR behavior of this elusive species (if any).

(50) (a) Slipchenko, L. V.; Munsch, T. E.; Wenthold, P. G.; Krylov, A. I. *Angew. Chem., Int. Ed.* **2004**, *43*, 742–745. (b) Krylov, A. I. *J. Phys. Chem. A* **2005**, *109*, 10638–10645. (c) Koziol, L.; Winkler, M.; Houk, K. N.; Venkataramani, S.; Sander, W.; Krylov, A. I. *J. Phys. Chem. A* **2007**, *111*, 5071–5080.

(51) (a) Tuononen, H. M.; Suontamo, R. S.; Valkonen, J.; Laitinen, R. S. *J. Phys. Chem. A* **2004**, *180*, 5670–5677. (b) Tuononen, H. M.; Suontamo, R. S.; Valkonen, J.; Laitinen, R. S.; Chivers, T. *J. Phys. Chem. A* **2005**, *109*, 6309–6317.

(52) Gordon, M. S.; Schmidt, M .W.; Chaban, G. M.; Glaesemann, K. R.; Stevens, W. J.; Gonzalez, C. *J. Chem. Phys.* **1999**, *110*, 4199–4207.

Conclusions

The SEEPR technique, used in conjunction with isotopic labeling, is shown to be an effective tool for the identification of transient binary S,N radicals. Investigations of the nature of the interconversion between S_4N_4 and $[S_3N_3]^-$ have revealed that the primary electron-transfer product for S_4N_4 decays with first-order kinetics. The decay of the primary electron-transfer product for $[S_3N_3]^-$ is less straightforward and may follow either first or second-order kinetics. In either scenario, a significant role may be played by the EPR-silent $[NS]^{\bullet}$ radical. SEEPR studies on ^{15}N and ^{33}S isotope-labeled S_4N_4 provide compelling confirmation of the identity of $[S_4N_4]^{-\bullet}$. However, it was not possible to detect $[S_3N_3]^{\bullet}$ by applying the SEEPR technique to the oxidation of the corresponding anion $[S_3N_3]^-$, confirming previous reports for the non-observation of this species by EPR spectroscopy. [3,3]-CAS calculations unequivocally established that the ground state of $[S_3N_3]^{\bullet}$ has distinct triradicaloid character.

Acknowledgment. Financial support from the Natural Sciences and Engineering Research Council-Canada (R.T.B. and T.C.), the Alberta Ingenuity Fund (T.L.R.) and the Academy of Finland (H.M.T.) is gratefully acknowledged. We thank the NSERC for the purchase of the EPR spectrometer, and the University of Lethbridge for the potentiostat. We would also like to thank Drs. Stephen Feldberg; Manfred Rudolph, and an anonymous referee for help with the digital simulations and Dr. Keith Preston for advice on EPR spectra of $[S_3N_3]^{\bullet}$.

Supporting Information Available: Crystallography details for [PPN][$S_3N_3 \cdot HOCH_3$] (Figure S1, Table S1); CV conc. dep. for red. of S_4N_4 (Table S2); CV conc. dep. for ox. of $[S_3N_3]^-$ (Table S3); EPR spectrum of $S_4N_4^{-\bullet}$ at RT (Figure S2); first-order rate constants vs temp. for $[S_4N_4]^{-\bullet}$ (Table S4); simulated EPR spectra for $[S_3N_3]^{\bullet}$ (Figure S3); first-order rate constants vs temp. for $[S_4N_4]^{-\bullet}$ (Figure S4); half-lives vs temp. for $[S_4N_4]^{-\bullet}$ (Figure S5); plot of ln k versus $1/T$ for S_4N_4 (Figure S6); exptl. and simulated CF for S_4N_4 (Figure S7); parameters from simulating the $[S_4N_4]^{-/0}$ couple (Table S5); sensitivity of $[S_3N_3]^-$ toward oxygen; CVs for oxidation of $[S_3N_3]^-$ (Figure S8); exptl. and simulated CVs for [Cp_2Co][S_3N_3] (Figure S9); exptl. and simulated CVs for [PPN][S_3N_3] (Figure S10); parameters from simulating the $[S_3N_3]^{-/0}$ couple (Table S6); half-life for a second order reaction; PBE1PBE/(aug)cc-pVTZ geometry for a face-to-face dimer of $[S_3N_3]^{\bullet}$ (Figure S11). PBE1PBE/(aug)cc-pVTZ geometry of [*cyclo*-S_3N_3−N=S]$^{-\bullet}$ (Figure S12). This material is available free of charge via the Internet at http://pubs.acs.org.